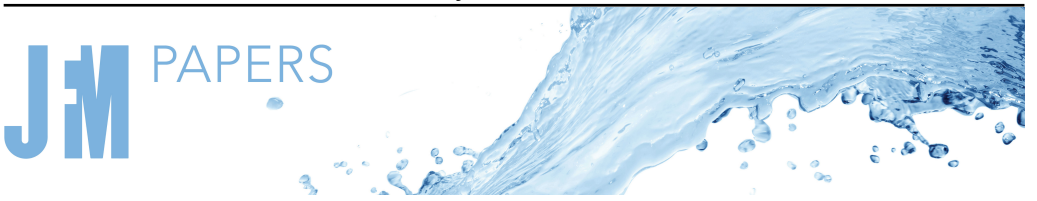
J. Fluid Mech. (2026), *vol.* 1033, A6, doi:10.1017/jfm.2026.11410



Bubble coalescence dynamics in a high-Reynolds number decaying turbulent flow

Vivek Kumar[1], **Prasoon Suchandra**[1], **Ardalan Javadi**[1], **Suhas S. Jain**[1] and **Cyrus K. Aidun**[1]

[1]George W. Woodruff School of Mechanical Engineering, Georgia Institute of Technology, Atlanta, GA 30332, USA

Corresponding author: Cyrus K. Aidun, cyrus.aidun@me.gatech.edu

(Received 4 September 2025; revised 24 January 2026; accepted 3 March 2026)

This study experimentally investigates bubble size evolution and void fraction redistribution in an unexplored, coalescence-dominated regime of a decaying turbulent bubbly flow. The flow is generated downstream of a regenerative pump in a duct, with bulk Reynolds number (Re) $\sim \mathcal{O}(10^5)$, Taylor-scale Reynolds number (Re_λ) $\sim \mathcal{O}(10^3)$ and void fraction (ϕ) $\sim \mathcal{O}(1\,\%)$, where the inlet turbulence is extremely intense (turbulence intensity $> 30\,\%$) but decays rapidly along the duct. Shadowgraph imaging and particle shadow velocimetry are used for measurements. The experimentally obtained turbulent dissipation in the duct flow decays as $\varepsilon \sim \mathcal{L}^{-2}$, where $\mathcal{L}$ is the axial position, in close agreement with the homogeneous isotropic turbulence prediction of $\varepsilon \sim \mathcal{L}^{-2.2}$. High-speed imaging and statistical analysis reveal that bubble coalescence dominates over breakup across most of the domain, leading to monotonic growth in the Sauter mean diameter (d_{32}) and progressive broadening of the bubble size distribution. The normalised extreme-to-mean diameter ratio ($\mathcal{D}$) increases axially and asymptotically from $\sim$1.9 (breakup regime) and saturates at $\sim$2.2 (coalescence regime), indicating the emergence of a quasi-self-similar bubble size distribution. The probability density function of the bubble diameter exhibits a dual power-law tail with exponents $-10/3$ and $-3/2$ near the duct inlet. However, after a few hydraulic diameters, a single $-3/2$ power-law scaling emerges, indicating a regime of pure coalescence in which all bubbles are smaller than the Hinze scale. The cumulative distribution plotted against d/d_{32} shows that the slope decreases and the distribution width increases with both axial position and void fraction (ϕ). Although classical Hinze scaling gives $d_H \propto \mathcal{L}^{0.9}$, our theory for d_{32} and $d_{99.8}$ (99.8th percentile bubble diameter) in a pure-coalescence regime predicts the slower law $\propto \mathcal{L}^{0.5}$, which our experimental results confirm – indicating negligible breakup and sub-Hinze growth. Concurrently, in contrast to current models, transient ϕ profiles evolve from nearly

© The Author(s), 2026. Published by Cambridge University Press. This is an Open Access article, distributed under the terms of the Creative Commons Attribution licence (https://creativecommons.org/licenses/by/4.0/), which permits unrestricted re-use, distribution and reproduction, provided the original article is properly cited.

https://doi.org/10.1017/jfm.2026.11410 Published online by Cambridge University Press

uniform to sharply core-peaked Gaussian distributions in the developing regime, with increasing centreline values and decreasing near-wall values, due to lift-force reversal. These results provide the first spatially resolved characterisation of coalescence-dominated bubbly flows at high *Re*, advancing the design of industrial systems as in nuclear cooling and multiphase forming processes (e.g. paper manufacturing, chemical reactors).

Key words: bubble dynamics, breakup/coalescence, gas/liquid flow

1. Introduction

Multiphase turbulent flows, where gases and liquids mix, are ubiquitous in industrial processes and natural phenomena. In applications ranging from chemical reactors and oil–gas pipelines (Delnoij *et al.* 1997) to oceanic wave breaking (Deane & Stokes 2002), the interaction of bubbles with turbulence critically affects mass transfer, reaction rates (Clift, Grace & Weber 2005) and flow behaviour. For example, the coalescence and breakup of bubbles in turbulence governs interfacial area and influences efficiency in systems like emulsifiers, heat exchangers and wastewater aeration tanks (Coulaloglou & Tavlarides 1977; Martínez-Bazán *et al.* 1999). High-Reynolds-number bubbly flows are especially important in devices such as multiphase pumps, where intense turbulence is deliberately generated to disperse gas into liquid (Javadi, Kumar & Aidun 2026). In such pump operations, bubbles can significantly alter performance: their formation, coalescence and breakup can enhance mixing, but also cause loss of efficiency if not controlled (Kolmogorov 1949; Hinze 1955; Javadi *et al.* 2026). For instance, in a multiphase pump impeller, strong turbulence fragments bubbles into smaller bubbles and influences the downstream two-phase flow (Zhang *et al.* 2018). Given the prevalence of bubbles in turbulence in engineering (e.g. bubble columns, pipelines, nuclear coolant loops) and in natural phenomena (e.g. breaking waves, volcanic eruptions), understanding coalescence/breakup dynamics under extreme turbulence is both fundamentally and practically important (Liao & Lucas 2009, 2010).

Quantifying the bubble size distribution is essential because it determines how bubbles partition across small and large sizes. A modified Gaussian function is commonly used, since it locates the most probable size, bounds the upper tail (e.g. $d_{\max}$) and measures the spread about the mean. These statistics are critical in systems such as (i) chemical bubble and slurry reactors (Kulkarni 2007), (ii) bioreactors and wastewater aeration (Kantarci, Borak & Ulgen 2005; Garcia-Ochoa & Gomez 2009), (iii) mineral flotation and dissolved air flotation processes (Wang *et al.* 2020), and (iv) CO_2 absorption and scrubbing (Chen *et al.* 2023). The bubble size distribution strongly influences process behaviour. It controls mass-transfer layers and current stability in electrochemical systems (Taqieddin *et al.* 2017; Angulo *et al.* 2020), delays slug formation and regulates pressure drop in gas-lift risers and pipelines (De Temmerman *et al.* 2015; Diaz, Gonzalez & Vera 2024), and enhances near-wall renewal in membrane air scouring at fixed aeration power (Fabre & Liné 1992; Alameedy *et al.* 2025). In practice, the ratio between extreme and mean sizes becomes particularly informative: lower ratios stabilise current density and reduce electrode coverage by large bubbles, while bounding this ratio in pipelines helps maintain bubbly or churn flow and delays slug initiation (De Temmerman *et al.* 2015; Kumar *et al.* 2023; Diaz *et al.* 2024). In membrane systems, tuning this ratio increases renewal at the wall without promoting excessive fouling (Fabre & Liné 1992; Alameedy *et al.* 2025).

The bubble size distribution mainly depends on two factors: coalescence and breakup in the turbulent flow. Numerically, the bubble size distribution is obtained by solving a

https://doi.org/10.1017/jfm.2026.11410 Published online by Cambridge University Press

population-balance equation coupled to the turbulent flow field, where coalescence and breakup kernels, formulated from theoretical models and closed empirically, govern the redistribution of bubbles across sizes in space and time (Lehr, Millies & Mewes 2002). These mechanisms have been extensively studied theoretically and computationally in turbulent environments, where energy dissipation, inertial forces and interfacial dynamics dictate the evolution of the bubble size distribution (Li & Liao 2024; Li *et al.* 2024). Bubble breakup in turbulence arises when inertial stresses exceed surface tension, fragmenting bubbles above a critical Weber number (We_{crit}) (Kolmogorov 1949; Hinze 1955; Ni 2024). The turbulence-based definition of the bubble Weber number is directly linked to the Kolmogorov description of breakup:

$$We = 2.13\,\frac{\rho_\ell}{\gamma}\,(\varepsilon d)^{2/3}\,d. \tag{1.1}$$

Here d is the bubble diameter, ε is the turbulent energy dissipation rate per unit mass, γ is the interfacial tension and ρ_ℓ is the density of the continuous phase (Salibindla *et al.* 2020). The Weber number corresponding to the maximum bubble size under given flow conditions is defined as the critical Weber number, We_{crit}, and the corresponding bubble diameter (d) is defined as the Hinze-scale diameter (d_H) (Hinze 1955; Hesketh, Etchells & Russell 1987). Experiments by Martínez-Bazán *et al.* (1999) showed a two-regime breakup frequency: rising near the critical size and decreasing for very large bubbles. Na, Chang & Lim (2022) reported a turbulence-driven power-law size distribution in oceanic flows. Direct numerical simulation (DNS) studies revealed further detail: Vela-Martín & Avila (2022) demonstrated memoryless breakup even for sub-Hinze droplets, while Calado & Balaras (2024) highlighted enhanced deformation when bubble size matches energy-containing eddies. Models by Prince & Blanch (1990), the energy cascade framework by Nambiar & Gandhi (1990), and Li & Liao (2024)'s turbulence modulated breakup relate breakup rates to turbulent dissipation and deformation. High Reynolds numbers amplify breakup via increased shear and energy cascade to small scales (Sajjadi *et al.* 2013; Chen *et al.* 2021), making the Weber number central to predicting fragmentation (Li & Liao 2024), with bulk-phase dissipation further modulating breakup dynamics (Nguyen *et al.* 2013).

Bubble coalescence in turbulent flows is governed primarily by collision frequency and coalescence efficiency (Scarbolo, Bianco & Soldati 2015). Early foundational models, such as Coulaloglou & Tavlarides (1977), introduced population-balance frameworks based on turbulent eddy collisions and liquid-film drainage mechanisms, establishing a fundamental framework for modelling bubble coalescence. Guo *et al.* (2016) and Prince & Blanch (1990) further developed this approach by distinguishing between collision frequency and coalescence efficiency, explicitly incorporating turbulence, buoyancy and viscous shear effects into their coalescence kernel. The Luo & Svendsen (1996) model refines these approaches by explicitly incorporating turbulence dissipation scales into predictions of collision and coalescence efficiency through film drainage modelling, proving especially effective at high void fractions (Nambiar & Gandhi 1990; Luo & Svendsen 1996). The recently developed interfacial area transport equation (IATE) further categorises coalescence events into random collisions, wake-entrainment events and hydrodynamic instabilities, offering a comprehensive framework widely accepted for detailed analyses of bubble interactions (Kamp, Chesters & Colin 2001). In practical computational fluid dynamics (CFD) simulations, these coalescence kernels are often embedded within the multi-size group (MUSIG) framework, in which the bubble population is discretised into size classes and a set of coupled population-balance equations is solved, enabling simultaneous prediction of bubble growth, breakup

https://doi.org/10.1017/jfm.2026.11410 Published online by Cambridge University Press

and redistribution across the bubble size spectrum (Kamp *et al.* 2001). Alternative approaches include energy-based models, such as Sovova's energy model, which postulates coalescence when the kinetic energy of colliding bubbles surpasses their surface energy (Liao & Lucas 2010). Liao & Lucas (2010) expanded this concept, advocating its direct applicability under turbulent conditions to emphasise the kinetic energy and surface energy balance during collisions. With empirical closures, these models have been incorporated into CFD through population-balance formulations, where the coalescence kernels are solved together with the flow field. Numerous studies have compared different combinations of breakup and coalescence models in simulations of bubbly systems such as bubble columns and stirred reactors (Matiazzo *et al.* 2020). For example, Laakkonen *et al.* (2005, 2006, 2007*b*) validated several models against experiments in moderately turbulent stirred vessels, using MUSIG approaches to reproduce bubble size distributions (Kamp *et al.* 2001; Matiazzo *et al.* 2020).

In extremely high turbulent flows, the bubble collision frequency increases markedly as elevated turbulent kinetic energy and fluctuating eddies generate rapid relative motion and frequent encounters between bubbles (Serizawa, Kataoka & Michiyoshi 1975; Lance & Bataille 1991). However, high shear forces and fluctuating velocities shorten the contact time during collisions, reducing coalescence efficiency by impeding liquid-film drainage and stabilising the intervening film (Hagesaether *et al.* 2000; Liao & Lucas 2010). Wake-entrainment effects, in which larger bubbles induce secondary flow structures, further influence local bubble distributions and enhance collision heterogeneity. As a result, turbulence simultaneously promotes collisions while suppressing net coalescence, creating a regime in which frequent impacts do not necessarily lead to merging (Lance & Bataille 1991; Hagesaether *et al.* 2000; Laakkonen *et al.* 2007*a*; Liao & Lucas 2010). These phenomena highlight the need to refine traditional coalescence models to account for the dual role of turbulence and the complex interplay between collision frequency, coalescence efficiency and flow structures in high-Reynolds-number multiphase flows (Laakkonen *et al.* 2007*a*).

Although widely used, these coalescence models exhibit fundamental limitations when applied to the extreme, rapidly evolving turbulence encountered downstream of pumps and injectors (bulk $Re = V\mathrm{D}/\nu \sim 10^5$ and $Re_\lambda = \mathcal{U}\lambda_T/\nu \sim 10^3$, where V is the bulk mean velocity, D is the hydraulic diameter of the duct, ν is the kinematic viscosity, $\mathcal{U}$ is the root-mean-square (r.m.s.) velocity fluctuation and λ_T is the Taylor microscale). Such flows are characterised by intense, strongly non-homogeneous turbulence, with local turbulence intensities approaching 50 %, followed by rapid axial decay (Javadi *et al.* 2026). Classical population-balance formulations, including Coulaloglou & Tavlarides (1977) and Prince & Blanch (1990) kernels, assume locally homogeneous, quasi-steady turbulence and rely on drainage and collision closures calibrated primarily under moderate conditions. As a result, they fail to capture the sharp spatial gradients in turbulence and the rapid evolution of the bubble size distribution in developing bubbly flows. The Luo & Svendsen (1996) film drainage model incorporates ε explicitly, but still presumes scale-invariant turbulence and near-equilibrium bubble interactions, assumptions that break down when the turbulent time scales evolve faster than the drainage dynamics. Energy-based criteria (e.g. Sovová-type models) further idealise coalescence as a simple kinetic–surface energy balance, neglecting interfacial rheology and transient film dynamics that become increasingly important at high Re. Even IATE- and MUSIG-based approaches ultimately depend on empirical source terms tuned for steady or weakly evolving flows, and thus, remain unvalidated in regimes where turbulence and bubble sizes change by orders of magnitude over short distances (Kamp *et al.* 2001). Experimental datasets under such extreme, decaying turbulence are correspondingly scarce, and most prior work

https://doi.org/10.1017/jfm.2026.11410 Published online by Cambridge University Press

has focused on either weak-to-moderate turbulence or idealised configurations such as homogeneous-grid turbulence, pseudo-turbulent bubble swarms or confined Hele-Shaw systems, leaving the coupled effects of strong turbulence decay, intense coalescence and evolving hydrodynamic interactions largely unresolved (Bouche *et al.* 2012, 2014).

The present study provides a first-of-its-kind experimental insight into bubble dynamics in a square duct under extreme pump-driven turbulence (bulk $Re > 10^5$ and $Re_\lambda \approx 900$). In this unique flow configuration, very high inlet turbulence intensity ($\mathcal{I} \gtrsim 30\,\%$) fragments incoming bubbles to sizes near the classical Hinze scale, in equilibrium with the effect of breakup and coalescence (Hinze 1955; Martínez-Bazán *et al.* 1999). As the flow convects downstream, turbulence decays rapidly along the axial direction. From (1.1), the Hinze scale satisfies $d_H \propto \varepsilon^{-2/5}$ and, therefore, increases as the turbulence decays. However, changes in bubble diameter are not governed solely by turbulence decay; they also depend on bubble size, void fraction and the initial bubble size distribution (Prince & Blanch 1990). As $\varepsilon(t)$ decreases, the bubble population progressively shifts toward coalescence-dominated growth, while the Hinze diameter d_H still limits the largest bubbles, since bubbles exceeding d_H undergo breakup. Thus, despite the rapid decay of turbulence downstream, the high collision frequencies near the inlet drive sustained coalescence, producing a gradual transition from pump-induced fragmentation to coalescence-driven growth. This strongly coalescent regime in a decaying turbulent flow has not been previously quantified (Ruth *et al.* 2022), and it highlights that models validated at a fixed turbulence level cannot be directly applied when ε decays over orders of magnitude in a short convective time. Consequently, it becomes essential to characterise bubble population dynamics in detail, including bubble size growth or decay (d, d_{32}, $d_{99.8}$), together with the spatial and temporal redistribution of bubbles.

The paper proceeds as follows. Section 2 describes the flow loop, design of experiments, control variables and operating conditions (gas volume fraction, bulk velocity). Section 3 outlines the measurement methods – shadowgraph imaging for bubble detection/tracking and particle shadow velocimetry (PSV) for the turbulent field and the computation of bubble statistics. Section 4 reports axial/radial trends in bubble size distributions and turbulence, the shift from breakup- to coalescence-dominated regimes and links to turbulence decay and dissipation, with comparisons to theory. Section 5 summarises key findings and implications for modelling extreme-turbulence multiphase flows. Experimental conditions are compiled in figure 2(*a*); symbols and acronyms appear in table 4.

2. Experimental set-up and procedure

A schematic of the experimental set-up is presented in figure 1. The flow loop begins at a 100-gallon conical stainless-steel tank (Diboshi, 100 gallon conical fermenter) filled with tap water. The tank connects via a flexible tubing (internal diameter: 17.80 $\pm$ 0.02 mm, length $\approx$1 m) to the suction side of pump I, a centrifugal pump (Dayton, PPLTAF23TDEG), whose speed is controlled by a variable frequency drive (VFD; Invertek drives, ODE-3-320153-1042). The outlet of pump I is connected to a Coriolis mass flow meter (Krohne MFM 4085K Corimass, type 300G+), shown as 'flow + pressure sensor' in figure 1, via a 1 m segment of the same 17.80 $\pm$0.02 mm tubing. Downstream, the flow enters a short polycarbonate circular duct (ID 17.80 $\pm$0.02 mm, length 15.24 $\pm$ 0.03 cm) divided into two sections and connected via a 1 inch (2.54 cm) NPT T-junction. An inline stainless-steel sparger of 1/4 inch (6.35 mm) NPT (2308-A04(00)-06-A00-GAS-AB, Moto Corp.) is installed in the direction of the flow, enabling aligned air injection. Compressed air is supplied through this sparger from a high-pressure compressor (maintained at 8 bar), regulated by a calibrated mass flow controller (Omega,

https://doi.org/10.1017/jfm.2026.11410 Published online by Cambridge University Press

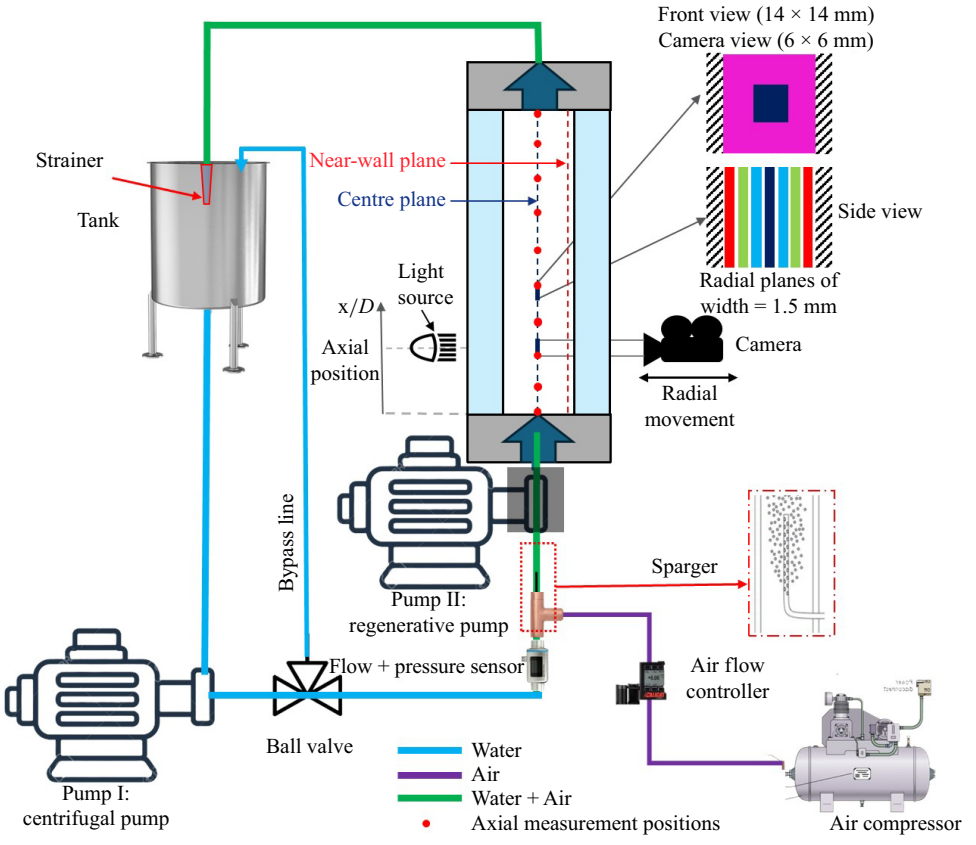


Figure 1. Schematic of experimental set-up and flow loop. Red discs: ten axial positions. Front view: channel cross-section 14 × 14 mm (magenta); visualisation window 6 × 6 mm (dark blue). Side view: measurements in seven radial planes from the near wall (red) to the centre plane (dark blue), each 1.5 mm wide.

FMA-A2309) placed in the supply line to regulate the injection rate precisely. This air–water mixing region is designed to align air injection with the bulk liquid flow and ensure fine initial dispersion.

Following the circular mixing duct, the flow enters pump II, a regenerative turbine pump (MTH Pumps, model E51M SS), via another segment of 17.80 ±0.02 mm tubing. Pump II is independently controlled using a dedicated VFD to maintain desired flow rates by adjusting motor frequency. To ensure the validity and independence of the set-up, experiments were repeated with three different impellers, and the results were consistent with those reported here. The discharge of pump II feeds into the test section – a vertical, square cross-sectional duct of internal dimensions 13.97 ± 0.03 mm × 13.97 ± 0.03 mm and a height of 60.96 ± 0.30 cm (aspect ratio 40). This duct is constructed from a rigid polycarbonate frame sandwiched between two optically clear 95 % transparent polycarbonate panels, allowing full optical access along the axial length for flow visualisation and measurement. Bubble size measurements were performed at multiple axial positions ($x/D = \mathcal{L} = 3.6{-}40$, where D is the hydraulic diameter of the duct, $D =$ 13.97 mm) and four radial locations (centreline, near wall and intermediates) using shadowgraph-based imaging. A high-speed camera (Photron FASTCAM Nova R2) equipped with a high-magnification lens (Navitar Resolv4K) and synchronised with a halogen backlight (OSL2, Thorlabs) was used to capture the bubble field. The camera

https://doi.org/10.1017/jfm.2026.11410 Published online by Cambridge University Press

(*a*)

$\mathcal{L}$	Q (V) L/min (m s^{-1})	ϕ (%)	Re ($\times 10^4$)	Re_λ ($\mathcal{L} \approx 0$)
0, 3.6, 8.2, 12.7, 17.8, 21.8, 26.4, 30.9, 35.5, 40.0	72 (6.1)	0.5 1 2	9.4	583
	87 (7.4)	0.5 1 2	11.4	825
	98 (8.4)	0.5 1 2	12.9	918

(*b*)

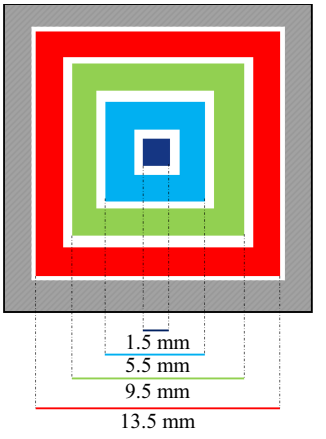


Figure 2. (*a*) Experimental conditions, including axial positions ($\mathcal{L}$), flow rates (Q), bulk velocity (V), void fraction (ϕ), bulk Reynolds number ($Re = VD/\nu$) and Taylor Reynolds number ($Re_\lambda = \mathcal{U}\lambda_T/\nu$), where D is the duct hydraulic diameter, ν is the liquid kinematic viscosity, $\mathcal{U}$ is the root-mean-square (r.m.s.) value of the velocity fluctuations and λ_T is the Taylor microscale. (*b*) Radial measurement locations in a 14 mm × 14 mm duct region. Each measurement plane (red (near wall), green, sky blue, dark blue (centre)) is 1.5 mm thick and separated by 0.5 mm white spacing, and the wall to red plane clearance is 0.25 mm.

was interfaced with a data acquisition system to record high-resolution images at each measurement location. Particle shadow velocimetry (Estevadeordal & Goss 2005; Khodaparast *et al.* 2013; Hessenkemper & Ziegenhein 2018; Jassal, Song & Schmidt 2025) was employed in parallel using a similar visualisation window to estimate turbulence statistics, including velocity fields, turbulent kinetic energy (k), turbulence intensity ($\mathcal{I}$) and dissipation rate (ε) .

The outlet of the test section is connected to a return line that recirculates the two-phase mixture back into the storage tank. A fine mesh strainer (4856K221, McMaster-Carr) is placed at the return to prevent large air slugs from re-entering the suction line. To ensure minimal air entrainment into pump I, the return line terminates with a vertically mounted perforated bottle within the tank, which facilitates the complete separation of entrained air from the returning water. The tank's large cross-sectional area further aids in the natural escape of bubbles, while ensuring a bubble-free inlet condition at the pump suction. The absence of air entrainment was verified by capturing high-speed images under no-air-injection conditions. Thermal effects were minimal throughout the experiments. The only source of heat was viscous dissipation due to wall shear. The initial water temperature was maintained at 20 °C and continuously monitored. If the temperature deviated from 20 ± 2 °C during extended operation, the water was drained and replaced to ensure thermal consistency across all measurements.

The experiments were conducted to investigate bubble dynamics in a highly turbulent, decaying duct flow over a broad range of operating conditions, as shown in figure 2(*a*). Three bulk velocities, corresponding to volumetric flow rates (Q) of 72, 87 and 98 L min^{-1} (6.1–8.4 m s^{-1}), yielded bulk Re of 9.4×10^4, 1.14×10^5 and 1.29×10^5. For each velocity, three inlet void fractions ($\phi = Q_{air}/Q = Q_{air}/Q_{air} + Q_{liquid} = 0.5,\ 1,\ 2\ \%$) were varied; Q_{air} here indicates air flow rate. Measurements were performed at ten axial positions spanning $x = 0{-}40D$, capturing the progressive evolution of the two-phase flow as turbulence decayed downstream. The corresponding Taylor-scale Reynolds number Re_λ near the inlet ranged from 583 to 918. Radial variations were resolved at four discrete interrogation windows as seen in figure 2(*b*).

https://doi.org/10.1017/jfm.2026.11410 Published online by Cambridge University Press

3. Measurement techniques

3.1. *Shadowgraph for bubble imaging*

A high-speed imaging system was utilised to capture bubble dynamics within the designated observation sections (figure 1). The set-up featured the same camera and a halogen backlight, ensuring uniform and high-contrast visualisation of the bubbles. Imaging was performed at 0.64× optical magnification with a shutter speed of 3.33 µs, providing a spatial resolution of 2.9 ± 0.1 µm over a 6 × 6 mm^2 field of view. Image sequences were recorded in lossless TIF format at 1 frame per second (fps) intervals, which both maximised image fidelity and minimised the likelihood of repeated bubble detection during subsequent post-processing.

3.2. *Bubble imaging – calibration, data processing and uncertainty analysis*

The imaging system was calibrated using a reference wire strand of known diameter (250.0 ± 0.5 µm) positioned within a focal plane depth of 1.50 ±0.03mm. The resulting spatial resolution was ≈3 ±0.2 μm pixel^{-1} and the estimated positional accuracy for clearly resolved bubble edges was ±6 µm. The smallest detected bubbles had a diameter of approximately 10 μm. For isolated, in-focus bubbles, this corresponds to a diameter uncertainty of ±10–12 µm, while in cases involving overlapping or partially defocused boundaries, manual verification and correction limited the maximum uncertainty to ±15 µm. Quantitative image analysis was performed using a custom MATLAB-based algorithm. Raw frames shown in figure 3(*a*) were first preprocessed through background subtraction to suppress noise and enhance bubble edges. Bubble contours, as shown in figure 3(*b*), were detected using the Canny edge detection method (Rong *et al.* 2014), and Watershed segmentation (Seal, Das & Sen 2015) was applied to resolve overlapping bubbles. Furthermore, the bubble size distribution for select images was cross-validated using the open-source, deep learning-based automated bubble detection algorithm developed by Kim & Park (2021). The projected two-dimensional (2D) area A of each bubble was obtained from the shadowgraph images. Because only a single planar projection is available, the bubble size was defined using the area-equivalent diameter, i.e. the diameter of a circle with the same projected area A:

$$d = d_{equiv} = \left(\frac{4A}{\pi}\right)^{1/2}. \tag{3.1}$$

Over 2000 bubbles were analysed for each experimental condition to ensure statistical robustness. The minimum number of bubbles/images was chosen based on the convergence of all bubble-distribution, count and void fraction statistics, with $d_{99.8}$ computed as the mean diameter of the largest 0.5 % of bubbles to ensure a robust characterisation of the extreme tail. The Sauter mean diameter d_{32} was computed as

$$d_{32} = \frac{\sum_{i=1}^{N} d_i^3}{\sum_{i=1}^{N} d_i^2}, \tag{3.2}$$

where d_i is the bubble diameter and N is the total number of bubbles detected. To assess uncertainty in d_{32}, a sensitivity analysis was performed by varying segmentation thresholds and repeating the analysis on selected datasets. The relative uncertainty in d_{32} was estimated to be ±4–6 % (between repeated runs), primarily due to image processing variability and resolution limits. Using an area-equivalent diameter implicitly assumes approximate axisymmetry of the projected bubble shape. This assumption is justified here because the bubbles satisfy $We \lesssim 1$, so they are nearly spherical or only weakly

https://doi.org/10.1017/jfm.2026.11410 Published online by Cambridge University Press

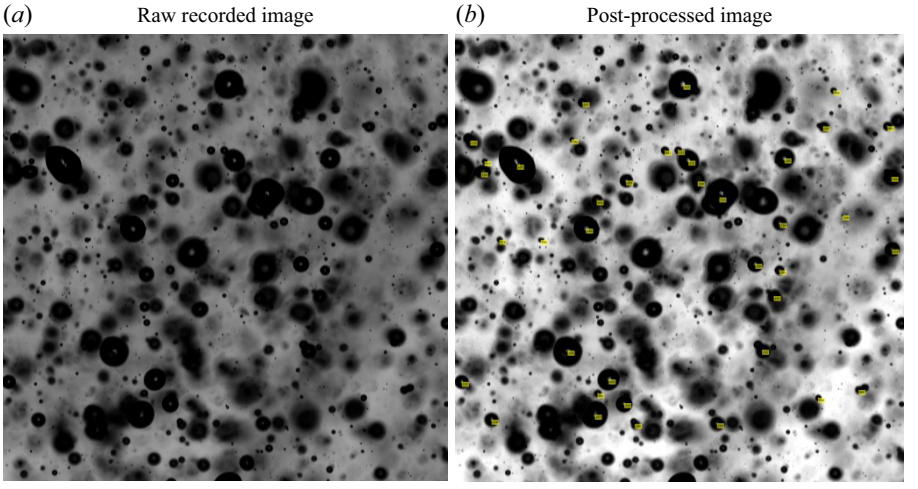


Figure 3. Image processing and bubble detection software (resized: 6×6 mm^2). (*a*) Raw recorded image, (*b*) post-processed image.

deformed. Under these conditions, the difference between the true projected area and its circular equivalent is typically below $\sim$5 %, as reported in previous studies (Risso & Fabre 1998; Zenit & Magnaudet 2008; Razzaque *et al.* 2003*b*). To ensure reproducibility, each experimental condition was repeated three times on different days. The variation in results (e.g. d_{32}, bubble count) across these trials remained within the reported uncertainty bounds, confirming the consistency and robustness of the measurement and processing methodology.

3.2.1. *Particle shadow velocimetry for turbulent field*

Particle shadow velocimetry provides a cost-effective, non-intrusive alternative to particle image velocimetry (PIV) for obtaining the flow velocity field (Estevadeordal & Goss 2005; Khodaparast *et al.* 2013; Hessenkemper & Ziegenhein 2018; Jassal *et al.* 2025). Particle shadow velocimetry was implemented to measure primarily the liquid-phase velocity in the vertical duct. A high-power tungsten-halogen light source (Thorlabs OSL2) back illuminated the flow from behind (see figure 1), casting sharp shadows of flow tracers onto the sensor of a high-speed Photron Nova R2 camera operated at 20 000 fps. The depth of field of the lens used is $\approx$0.5 mm, which is comparable to the typical laser-sheet thickness in planar PIV applications. The flow was seeded with nearly neutrally buoyant hollow glass spheres (mean diameter $\sim$ 10 μm), which serve as PSV flow tracers. The response time of these tracers/particles is much smaller than the characteristic flow time scale, i.e. Stokes number $\ll 1$, ensuring faithful tracking of the smallest turbulent motions. The calibrated field of view covered roughly 3 mm in the vertical direction at approximately 10 μm pixel^{-1} resolution. Note that the image resolution for PSV is lower than that for bubble imaging discussed previously. This was to capture sufficient particle and small bubble motions within the field of view. The PSV images (with both particle and bubble shadows) were processed, subtracting background and removing large bubble shadows, to convert them into formats suitable for cross-correlation based PIV processing (see figure 4). Image pairs were then processed with the open-source software OpenPIV (Liberzon *et al.* 2020). We used 128×128 pixel interrogation windows with 75 % overlap. Bubble shadows and any spurious large particles (high-Stokes tracers) were masked or excluded. The resulting instantaneous velocity fields were further checked and corrected

https://doi.org/10.1017/jfm.2026.11410 Published online by Cambridge University Press

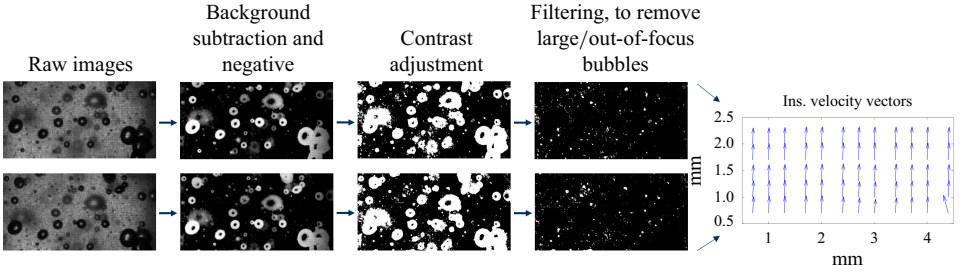


Figure 4. Different stages of image processing involved in PSV.

for spurious data using the universal outlier detection method of Westerweel & Scarano (2005). The velocity statistics converged beyond 500 image pairs and we conservatively used 1000 image pairs. The controlled nature and repeatability of our experiments and analyses were demonstrated by the close agreement in converged turbulence statistics obtained from multiple independent runs (each repeated at least three times), conducted at different times but under identical operating conditions. Compared with traditional laser-sheet PIV, PSV provides comparable accuracy for velocity and turbulence measurements in bubbly flows while avoiding complex optics and laser-light scattering issues (Jassal *et al.* 2025). The uncertainties in velocity and turbulence statistics were estimated using the methods of Wieneke (2015) and Sciacchitano & Wieneke (2016).

From the validated vector fields, we computed ensemble-averaged and fluctuation quantities, following the Reynolds decomposition of the velocity $u = \overline{u} + u'$. The mean velocity profile ($\overline{u}$) was obtained by ensemble averaging each instantaneous vector component (u). The two-component turbulent kinetic energy (k) and turbulence intensity ($\mathcal{I}$) were estimated from the instantaneous fluctuations (u'), as shown below in (3.3) to (3.5):

$$k = \frac{1}{2}\left(\overline{u'^2} + \overline{v'^2} + \overline{w'^2}\right). \tag{3.3}$$

In the duct core, the two transverse directions are geometrically equivalent, and both DNS and our measurements show that the transverse Reynolds normal stresses collapse closely, with differences between $\overline{v'^2}$ and $\overline{w'^2}$ typically below $\mathcal{O}(10\,\%)$ (Gavrilakis 1992; Owolabi, Poole & Dennis 2016). In this region, the approximation $\overline{w'^2} \approx \overline{v'^2}$ provides a convenient simplification of the k expression. Closer to the wall, the turbulence becomes more anisotropic and the difference between $\overline{v'^2}$ and $\overline{w'^2}$ may increase to $\sim$20 %. However, because k is dominated by the streamwise fluctuations ($\overline{u'^2} > \overline{v'^2}, \overline{w'^2}$), the impact of this approximation on k is small, and the use of $\overline{w'^2} \approx \overline{v'^2}$ introduces only a negligible bias in the present results. With $\overline{w'^2} \approx \overline{v'^2}$,

$$k \approx \frac{1}{2}\left(\overline{u'^2} + 2\,\overline{v'^2}\right). \tag{3.4}$$

The $\mathcal{I}$ can be evaluated as

$$\mathcal{I} = \frac{\mathcal{U}}{V} = \frac{\sqrt{\frac{2k}{3}}}{V}, \tag{3.5}$$

where V is bulk velocity. The time series of velocity fluctuations from the centre plane are used to compute energy spectra E (Pope 2000) and these are shown in figure 5 for the cases $\phi = 0\,\%$ and $\phi = 0.5\,\%$, at $\mathcal{L} = 0.9$ (inlet to the test section) and $\mathcal{L} = 3.6$, for bulk

https://doi.org/10.1017/jfm.2026.11410 Published online by Cambridge University Press

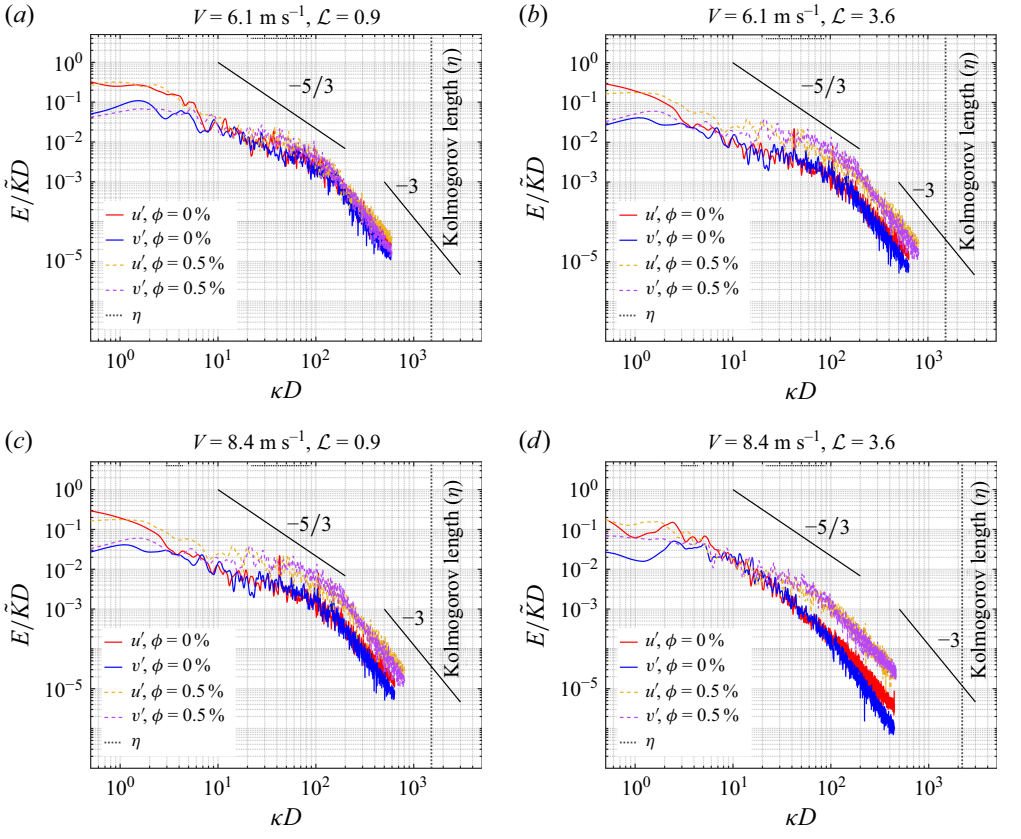


Figure 5. Energy spectra for u' and v' for $\phi = 0\,\%$ and $\phi = 0.5\,\%$, at $\mathcal{L} = 0.9$ and $\mathcal{L} = 3.6$, for the bulk velocities $V = 6.1$ m s^{-1} and $V = 8.4$ m s^{-1}. The vertical dotted line on the right indicates the expected Kolmogorov scale η. Kolmogorov–Obukhov's $\kappa^{-5/3}$ scaling (Kolmogorov 1941*a*,*b*; Obukhov 1941; Kolmogorov 1962; Obukhov 1962), representative of the inertial subrange of three-dimensional homogeneous, isotropic turbulence, is shown for comparison. A steeper '-3' slope, usually seen in the dissipation range (Brown & Bolotnov 2015; Lee 2020), is provided for reference; though our measurements do not directly resolve the dissipation range. Results are shown for (*a*) $V = 6.1$ m s^{-1}, $\mathcal{L} = 0.9$; (*b*) $V = 6.1$ m s^{-1}, $\mathcal{L} = 3.6$; (*c*) $V = 8.4$ m s^{-1}, $\mathcal{L} = 0.9$; (*d*) $V = 8.4$ m s^{-1}, $\mathcal{L} = 3.6$.

velocities $V = 6.1$ m s^{-1} and $V = 8.4$ m s^{-1}. Here κ indicates the wavenumber (frequency related to wavelength; see Taylor 1938) and $\tilde{K}$ is a wavelength scale (corresponding to sampling length). Our measurements resolve the intermediate length scales of turbulence, i.e. Taylor microscales ($\kappa D \sim 10^1 - 10^2$), and we observe close to Kolmogorov–Obukhov's $\kappa^{-5/3}$ scaling (Kolmogorov 1941*a*,*b*; Obukhov 1941; Kolmogorov 1962; Obukhov 1962) in the inertial subrange, suggesting the possibility of our flow approaching local isotropy. The $\kappa^{-5/3}$ scaling is representative of three-dimensional homogeneous, isotropic turbulence. A steeper '-3' slope, usually seen in the dissipation range (Brown & Bolotnov 2015; Lee 2020), is provided for reference in figure 5. However, we do not resolve the smallest scales of turbulence (Kolmogorov microscale η) in the dissipation range.

From figures 5(*a*) and 5(*c*) showing the spectra of fluctuations at the inlet to the test section, we see both streamwise (u') and radial (v') velocity fluctuations showing very similar behaviour through the inertial subrange, for both $\phi = 0\,\%$ and $\phi = 0.5\,\%$ cases for both bulk velocities, suggesting a nearly homogeneous, isotropic behaviour of the flow

https://doi.org/10.1017/jfm.2026.11410 Published online by Cambridge University Press

here at small scales. However, at large scales, as expected, the dominance of u' over v' is apparent in figure 5. As we move slightly downstream to $\mathcal{L} = 3.6$ (figures 5*b* and 5*d*), we find an enhancement of energy on small scales for the multiphase case ($\phi = 0.5\,\%$) when compared with the single-phase (liquid only) case ($\phi = 0\,\%$), leading to a less steep slope in spectra. Such an observation has been previously reported by van den Berg *et al.* (2006) for turbulent flows with small bubbles (of diameters $d \lesssim 20\eta$) when the bubblance (ratio of kinetic energy of bubble motion to fluctuations in liquid velocity) is small, and the bubble action on the flow is selective in wavenumber, with bubbles acting as forcing sources at small scales.

When looking at effects of different bulk velocities on spectra, we see the spectra for the higher bulk velocity ($V = 8.4$ m s^{-1}) showing slightly steeper, more uniform, closer to '$-5/3$' slopes in the inertial range than the lower velocity cases, as expected due to higher level of turbulence and greater separation of scales accompanying higher bulk velocity. As the Kolmogorov scale is larger for the $V = 6.1$ m s^{-1} case, our experiments resolve a larger portion of the range of scales for the lower bulk velocity cases. Another interesting observation is steepening of spectra for all the cases, at smaller scales. This is partially due to spectra approaching the dissipation range and partially due to filtering out experimental noise. The steepening is prominent for the lower velocity cases where spectra are closer to the Kolmogorov scale.

The measured dissipation rate (ε_m) is first calculated using the 2D velocity gradients, via

$$\varepsilon_{m,iso} = 3\nu\overline{\left(\frac{5}{6}\left(\frac{\partial u'}{\partial x}\right)^2 + \frac{7}{12}\left(\frac{\partial v'}{\partial x}\right)^2 + \frac{7}{12}\left(\frac{\partial u'}{\partial y}\right)^2 + \frac{5}{6}\left(\frac{\partial v'}{\partial y}\right)^2 - \frac{\partial u'}{\partial x}\frac{\partial v'}{\partial y} - \frac{\partial v'}{\partial x}\frac{\partial u'}{\partial y}\right)} \tag{3.6}$$

under the local isotropy assumption (Hinze 1975; Xu & Chen 2013; Verwey & Birouk 2022) and via

$$\varepsilon_{m,axi} = \nu\overline{\left(-\left(\frac{\partial u'}{\partial x}\right)^2 + 2\left(\frac{\partial v'}{\partial x}\right)^2 + 2\left(\frac{\partial u'}{\partial y}\right)^2 + 8\left(\frac{\partial v'}{\partial y}\right)^2\right)} \tag{3.7}$$

under the local axisymmetry assumption (George & Hussein 1991; Xu & Chen 2013). Although we get close estimates from both the approaches, the assumption of local axisymmetry is less restrictive and better suited for our flow geometry. Therefore, we use $\varepsilon_{m,axi}$.

As discussed earlier, due to the limited resolution of PSV used here, the dissipation rates obtained from measured velocity fields and velocity gradients are considerably underestimated (Lavoie *et al.* 2007; Xu & Chen 2013; Verwey & Birouk 2022). For the current work, we use the DNS-calibrated, structure function and spectra-based empirical method of Xu & Chen (2013) that corrects the measured dissipation rate ε_m as a function of Δ/η and estimates the corrected dissipation rate ε_{cor} as

$$\frac{\varepsilon_m}{\varepsilon_{cor}} = a_1 e^{a_2(\Delta/\eta)} + b_1 e^{b_2(\Delta/\eta)}, \tag{3.8}$$

where Δ is the PSV vector spacing, η is the Kolmogorov scale and $a_1 = 1.1910$, $a_2 = -0.03081$, $b_1 = -0.1835$, $b_2 = -0.2062$ for a top-hat interrogation window. Independently, the corrected dissipation was verified against the classical homogeneous isotropic turbulence (HIT) scaling ($\varepsilon \sim C_\varepsilon u'^3/\ell$, with a relative ratio of $C_\varepsilon \approx \mathcal{O}(1)$ and $\ell \sim$ hydraulic diameter D), and the resulting values (order of magnitude) fairly agree.

https://doi.org/10.1017/jfm.2026.11410 Published online by Cambridge University Press

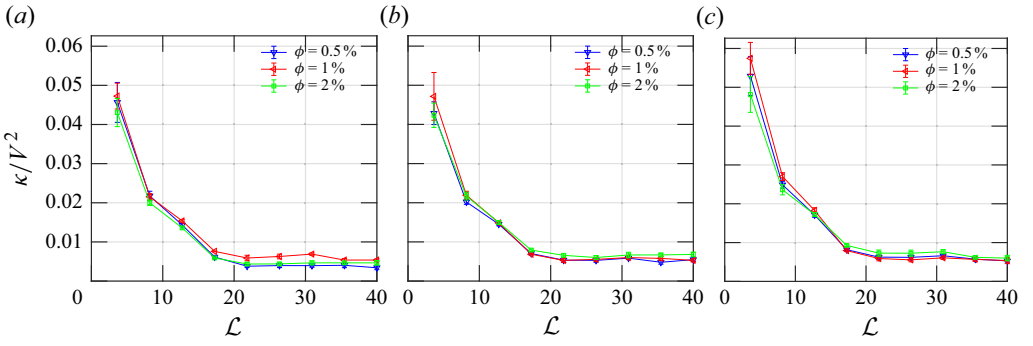


Figure 6. Axial variation of k along the duct centreline for three bulk velocities $V(Q)$ and three void fractions ϕ. Results are shown for (*a*) $V = 6.1\ \mathrm{m\ s^{-1}}$, (*b*) $V = 7.4\ \mathrm{m\ s^{-1}}$, (*c*) $V = 8.4\ \mathrm{m\ s^{-1}}$.

This is consistent with expectations for high-Reynolds-number developing turbulence (Sreenivasan 1984; Pope 2000; Valente & Vassilicos 2012).

4. Results and discussions

Section 4 provides a detailed characterisation of turbulence and bubble dynamics in the developing duct flow. The analysis covers the axial evolution of turbulent kinetic energy (k) and dissipation rate (ε), followed by a comprehensive examination of bubble size distributions through the modified Gaussian function, $f(d)$, cumulative distribution, $\Phi(d)$, and their scaling behaviour. Key statistical measures, including the Sauter mean diameter (d_{32}) and the extreme-to-mean size ratio ($d_{99.8}/d_{32}$), are quantified. Additionally, we study the influence of turbulence decay on the transition between coalescence- and breakup-dominated regimes, explore axial and radial variations in the local void fraction (ϕ), and establish scaling laws governing the evolution of bubble populations in high-intensity, decaying turbulence.

4.1. *Turbulent kinetic energy and dissipation rate*

The evolution of the turbulent velocity fields along the duct axis is critical for understanding bubble dynamics in developing flows. This spatial variation in turbulence directly governs the interplay between bubble breakup and coalescence, making its quantification essential for predicting bubble size evolution and optimising industrial multiphase flow systems (Li & Liao 2024). During the characterisation of our experimental set-up, near the inlet of the duct, we find that the incoming flow from the regenerative pump is nearly homogeneous, consistent with our large eddy simulation of the same pump (Javadi *et al.* 2026). We find that the mean streamwise velocity shows an almost flat radial profile across most of the cross-section, followed by a sharp decline confined to the near-wall region. The r.m.s. turbulent fluctuation profiles exhibit a similar trend: fluctuations remain relatively uniform in the core and increase toward the wall, consistent with classical observations of developing turbulent duct and pipe flows (Tavoularis & Corrsin 1981; Pope 2000).

In all our experimental cases presented here, the $\mathcal{I}$ imparted by the pump rapidly decreases as the flow develops. Figures 6 and 7 present the axial evolution of the estimates of centreline normalised turbulent kinetic energy (k/V^2) and normalised turbulent dissipation rate ($\varepsilon D/\bar{V}^3$) with $\mathcal{L}$ at different bulk velocities (V). The centreline k and ε both decrease by an order of magnitude (over $\sim$90 % reduction) from the inlet to the

https://doi.org/10.1017/jfm.2026.11410 Published online by Cambridge University Press

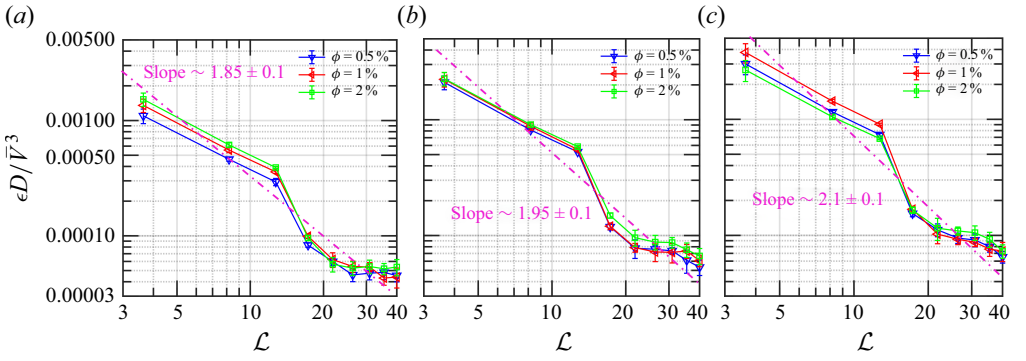


Figure 7. Axial variation of ε along the duct centreline for three bulk velocities $V(Q)$ and three void fractions ϕ. Note the use of the log–log scale. The range of the coefficient of determination (R^2) is provided. Results are shown for (*a*) $V = 6.1$ m s^{-1} (R^2: 0.94–0.97), (*b*) $V = 7.4$ m s^{-1} (R^2: 0.93–0.97), (*c*) $V = 8.4$ m s^{-1} (R^2: 0.93–0.95).

farthest measurement station. This steep initial decay reflects the absence of sustaining turbulence production in the core flow immediately after the pump, so the injected turbulent eddies dissipate energy quickly. Beyond ≈ 22 hydraulic diameters downstream, the rate of decline becomes much gentler (almost levelling off for the lowest bulk velocity case), indicating the approach toward a quasi-equilibrium turbulence state. At the lowest bulk velocity $V = 6.1$ m s^{-1}, for instance, ε drops very rapidly in the first few hydraulic diameters and then flattens by $\mathcal{L} \approx 30$ (suggesting that the core turbulence has largely equilibrated by that distance). In contrast, at the highest velocity ($V = 8.4$ m s^{-1}), centreline dissipation is still gradually decreasing even at the farthest location ($\mathcal{L} \approx 40$), implying a longer development length before fully developed conditions are reached. These observed trends – an initial exponential-like decay of turbulence followed by a slower power-law-like tail – are consistent with classical decaying turbulence behaviour downstream of intense turbulence sources, and they align with prior findings that high core turbulence decays rapidly in developing pipe flows until wall-driven production begins to dominate (Doherty *et al.* 2007; Wilson & Smith 2007). The locally steeper decay of ε for $\mathcal{L} \approx 12-18$ indicates a transition region where the inlet-imprinted turbulence rapidly adjusts to the duct confinement and developing shear, leading to a temporarily dissipation-dominated energy budget. Similar decay behaviour has been reported in other duct and pipe flows (Zikanov *et al.* 2019; Ding *et al.* 2021).

Increasing V significantly elevates both the centreline k and ε across the board. Flows at higher Re inject more energy into turbulence, yielding larger initial k and accordingly, higher ε values at the inlet and downstream. For instance, at $\mathcal{L} \approx 5$ the dissipation in the $V = 8.4$ m s^{-1} case is noticeably greater than in the $V = 6.1$ m s^{-1} case for the same air void fraction ϕ, and this gap persists downstream, although all cases eventually decay to significantly lower levels. Such a trend has been reported in other systems – e.g. Shawkat, Ching & Shoukri (2008) observed that the turbulence dissipation in horizontal bubbly flows rises with increasing V. Notably, the higher Re cases not only start with larger ε near the inlet, but also retain a higher dissipation level further downstream (since a more energetic flow takes longer to dissipate). The fact that the $V = 8.4$ m s^{-1} data in figure 7(*c*) still show a slight downward slope at $\mathcal{L} = 40$, whereas the $V = 6.1$ m s^{-1} data in figure 7(*a*) have nearly plateaued by that distance, suggests that the development length to reach a fully developed turbulence profile grows with Re. This is consistent with single-phase pipe flow

https://doi.org/10.1017/jfm.2026.11410 Published online by Cambridge University Press

literature – higher inertia flows require longer distances for turbulence redistribution and stabilisation, underscoring the significant influence of Re on turbulence evolution in our experiments (Doherty *et al.* 2007; Wilson & Smith 2007).

For the relatively low void fractions ($\phi = 0.5$–$2\,\%$) in the current study, the influence of ϕ on turbulence statistics is quite subtle. Any changes in the measured turbulent kinetic energy k and dissipation rate ε across this range remain within experimental uncertainty, in part because the PSV system lacks the fine-scale resolution to capture such small variations. Indeed, as shown in figures 6 and 7, the k and ε profiles at these low void fractions ϕ nearly overlap. This suggests that a threshold void fraction is required before bubbles appreciably augment the turbulence – a notion supported by prior studies. Lance & Bataille (1991) identified a regime at low void fraction where bubble–turbulence interactions are negligible, and Serizawa *et al.* (1975) likewise observed minimal turbulence modification at void fractions of the order of 1 %. Similarly, Shawkat *et al.* (2008) reported that at void levels of 1 %, any bubble-induced changes in turbulence are minor and often within the measurement scatter. Under the dilute conditions of the present study, therefore, the net impact of ϕ on k and ε is modest, and subtle bubble-induced enhancements cannot be reliably distinguished from experimental noise.

At the duct inlet, where the flow emerges directly from the pump, the turbulent kinetic energy imparted by the pump is initially distributed relatively uniformly across the pipe cross-section, resulting in elevated turbulent dissipation rates both at the centre and near the wall (refer to Appendices A and B). This high core dissipation arises from the injection of large-scale, isotropic turbulent eddies that permeate the bulk flow, a phenomenon frequently observed in turbulent flows downstream of energetic mechanical sources (Durst, Jovanović & Sender 1995; Pope 2000). In this region, turbulence production is not yet dominated by wall-shear effects, and the dissipation profile lacks the classical near-wall peak that is characteristic of fully developed pipe flows (Eggels *et al.* 1994). As the flow proceeds downstream, the imposed turbulence in the pipe core decays rapidly due to the absence of a sustaining production mechanism away from the wall (Pope 2000). In contrast, near-wall turbulence decays slower and is withheld by the strong mean velocity gradient at the solid boundary, which becomes the primary source of turbulent kinetic energy production and subsequent dissipation (Durst *et al.* 1995). Consequently, the radial dissipation profile evolves to exhibit a pronounced peak near the wall and a significant reduction at the centreline, reflecting the gradual transition from pump-driven, spatially uniform turbulence to a fully developed, wall-dominated turbulent regime (Eggels *et al.* 1994). This observed evolution aligns with established theoretical and experimental findings on the development of turbulence in wall-bounded shear flows and underscores the interplay between initial isotropic turbulence and the emergence of wall-driven turbulent structures.

Figure 7 shows that the turbulent dissipation decays approximately as a power law ($\varepsilon \propto \mathcal{L}^{-m}$) along the duct, appearing linear on a log–log plot with a best-fit slope m narrowly confined to $m \simeq 1.85$–2.10. The spread is small enough that the corresponding error bars largely overlap. This behaviour holds over most axial stations, except near the end where the growing wall boundary layer sustains turbulence and the decay becomes noticeably slower. As we see weak radial variations in our measurements, this scaling can be compared with theory by assuming HIT. In decaying HIT, the ε scaling follows a power law whose exponent is dependent on the large-scale invariant: where $k\ell^p = \text{constant}$ with $p \in \{3, 5\}$ (Batchelor & Proudman 1956; Saffman 1967). This implies that

$$k\ell^p = \text{constant} \quad \Rightarrow \quad \ell \propto k^{-1/p}, \tag{4.1}$$

https://doi.org/10.1017/jfm.2026.11410 Published online by Cambridge University Press

where ℓ is the integral length scale. For HIT,

$$\varepsilon \sim C_\varepsilon \frac{k^{3/2}}{\ell} \Rightarrow \varepsilon \propto k^{3/2+1/p}, \qquad \frac{\mathrm{d}k}{\mathrm{d}t} = -\varepsilon \Rightarrow \frac{\mathrm{d}k}{\mathrm{d}t} \propto -k^{m_t}, \tag{4.2}$$

where t is time and $m_t = 3/2 + 1/p$. Integration gives

$$k(t) \propto t^{-\frac{1}{m_t - 1}} = t^{-\frac{2p}{p+2}}, \tag{4.3}$$

$$\ell(t) \propto k^{-1/p} \propto t^{\frac{2}{p+2}}, \qquad \varepsilon(t) \propto \frac{k^{3/2}}{\ell} \propto t^{-\frac{3p+2}{p+2}}. \tag{4.4}$$

Simplifying for the case $t \to \mathcal{L}/\mathcal{V}$ gives

$$\varepsilon(t) \propto t^{-m_t} \propto \mathcal{L}^{-m_t}, \qquad m_t = \frac{3p+2}{p+2}. \tag{4.5}$$

The dimensionless time (t) is defined as $\mathcal{L}/\mathcal{V}$, where $\mathcal{V} = V/\bar{V}$ and $\bar{V} = V_1 + V_2 + V_3/3$. Thus, for a Saffman (1967) κ^2 spectrum ($p = 3$; permanence of big eddies for isotropic energy spectrum, $E(\kappa) \sim \kappa^2$ as $\kappa \to 0$; here κ is the wavenumber), one gets $\varepsilon \sim \mathcal{L}^{-2.2}$, while for a Loitsyanskii (1939) and Batchelor & Proudman (1956) κ^4 spectrum ($p = 5$), one gets $\varepsilon \sim \mathcal{L}^{-2.43}$. These theoretical scalings are broadly consistent and closely match with experimental measurements (see figure 7). A small but systematic discrepancy remains: the experimentally observed decay is slightly slower than the ideal HIT prediction, which is primarily due to wall-bounded effects in the duct that sustain dissipation and retard the streamwise decay, more pronounced near the end of the duct.

4.2. *Bubble size distribution and flow regime evolution*

The modified Gaussian function, $f(d)$, is widely used to compare and characterise the bubble size population (Friedlander *et al.* 2000). Controlling the mean/mode, σ, and $d_{\max}$ of the bubble size distribution in the flow is critical. Here $f(d)$ is represented by (4.6) and (4.7):

$$f(d) = \frac{\partial \Phi}{\partial \ln d} = \frac{1}{\sqrt{2\pi}\ln \sigma_g} \exp\left[-\frac{1}{2}\left(\frac{\ln(d/d_g)}{\ln \sigma_g}\right)^2\right], \tag{4.6}$$

where

$$d_g = \left(\prod_{i=1}^{K} (d_i)^{n_i}\right)^{\frac{1}{K}} \quad \text{and} \quad \ln \sigma_g = \sqrt{\frac{\sum_{i=1}^{K} n_i (\ln d_i - \ln d_g)^2}{N}}, \tag{4.7}$$

with d_i the representative diameter for bin i, n_i the number of bubbles in that bin, K the total number of bins, d_g and σ_g the geometric mean diameter and geometric standard deviation (Razzaque *et al.* 2003*b*) and Φ the cumulative fraction of bubbles with diameters smaller than d. Quantifying $f(d)$ is technically essential because, as established by the statistical framework of Friedlander *et al.* (2000), multiplicative coalescence–breakup processes impose integral constraints on the geometric mean d_g and variance σ_g, thereby allowing the net interaction rates in population-balance models to be inferred from the measured distribution. Figure 8 presents the experimentally measured bubble size distributions $f(d)$, constructed from the detected bubble diameters and shown on a semi-logarithmic scale. The curves represent log-normal fits evaluated using (4.6) and (4.7), with the parameters d_g and σ_g obtained directly from the measured data near the centre of the duct. Figure 8 ($a \to b \to c$, $d \to e \to f$) shows that increasing velocity (V), or Re, shifts the $f(d)$ toward a smaller mean and standard deviation of bubble size distribution.

https://doi.org/10.1017/jfm.2026.11410 Published online by Cambridge University Press

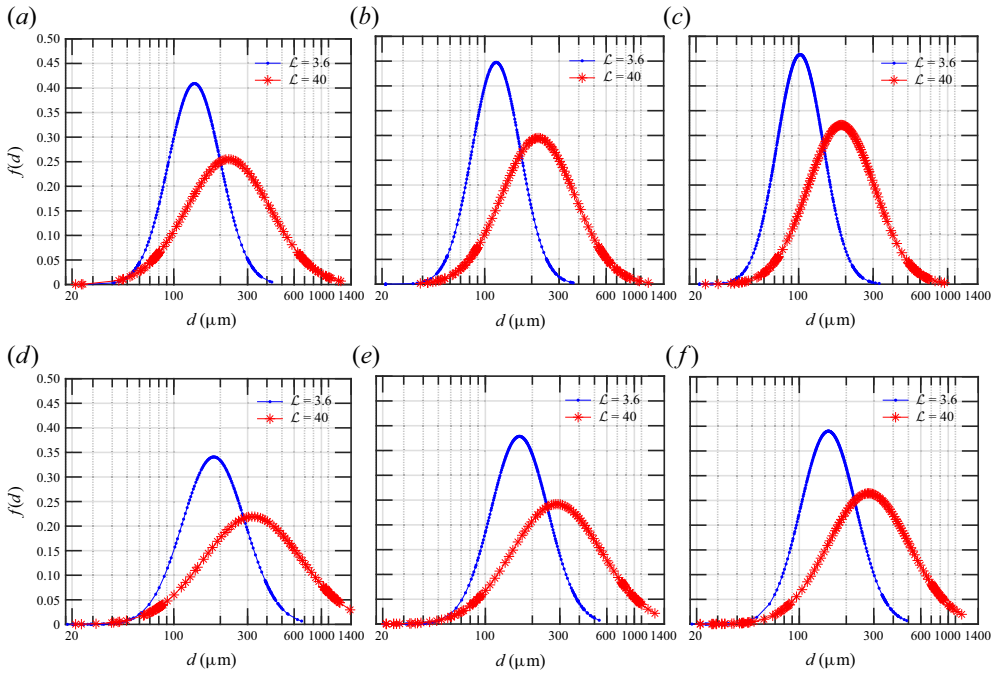


Figure 8. Bubble size distribution with modified Gaussian function $f(d)$ near the centre at different V and ϕ. Results are shown for (*a*) $V = 6.1\ \mathrm{m\ s^{-1}}$ and $\phi = 0.5\,\%$, (*b*) $V = 7.4\ \mathrm{m\ s^{-1}}$ and $\phi = 0.5\,\%$, (*c*) $V = 8.4\ \mathrm{m\ s^{-1}}$ and $\phi = 0.5\,\%$, (*d*) $V = 6.1\ \mathrm{m\ s^{-1}}$ and $\phi = 2\,\%$, (*e*) $V = 7.4\ \mathrm{m\ s^{-1}}$ and $\phi = 2\,\%$, (*f*) $V = 8.4\ \mathrm{m\ s^{-1}}$ and $\phi = 2\,\%$.

At the highest V ($8.4\ \mathrm{m\ s^{-1}}$), $f(d)$ exhibits a tall, sharp peak at a relatively small diameter, with a greatly diminished tail of large bubbles. In contrast, at the lowest V ($6.1\ \mathrm{m\ s^{-1}}$) the distribution is broader and more right-sided, with a noticeable tail consisting of larger bubbles. Physically, the more energetic turbulence at higher ε breaks bubbles into smaller sizes and rapidly fragments any large bubbles, yielding a narrower size spectrum (Prince & Blanch 1990). In fact, classic coalescence–breakup models of Prince & Blanch (1990) treat turbulence as the driver of bubble collisions, but sufficient contact time is required for coalescence. Extremely intense turbulence shortens bubble contact times, suppressing coalescence efficiency, so breakup prevails and limits the upper bubble size. This is in agreement with the observed disappearance of the large-diameter tail at the highest velocity.

Moving downstream in the duct (from $\mathcal{L} \simeq 3.6$ to 40 after injection) shown in figure 8(*a*,*b*,*c*,*d*,*e*,*f*) at given ϕ and V, the bubble size distribution progressively broadens and develops a less pronounced peak. Near the injection point ($\mathcal{L} \simeq 3.6$ downstream), $f(d)$ is relatively narrow with a small tail of both very small and a few large bubbles – a signature of the initial breakup of the air flow by the pump's turbulence. With an increase in $\mathcal{L}$ (shown for $\mathcal{L} = 40$ in figure 8), the distribution becomes broader around a modal diameter and the extreme (specifically very large bubbles) are more prevalent. This broadening of the distribution reflects the combined effects of decaying turbulence and ongoing bubble–bubble interactions. As the turbulence energy dissipates downstream, fewer new microbubbles are generated by breakup, and the small bubbles present begin to coalesce into mid-sized ones. The net result is an evolving equilibrium toward coalescence: the overall bubble count decreases with distance, indicating that many small bubbles are merging into larger ones. Notably, the large bubble tail of the distribution grows

https://doi.org/10.1017/jfm.2026.11410 Published online by Cambridge University Press

significantly by $\mathcal{L} \sim 40$, suggesting that large bubbles are formed via coalescence in the still turbulent (though weakening) flow. Thus, with downstream distance the bubble population shifts toward larger characteristic diameters, as an initially narrow distribution broadens and the peak amplitude decreases. Similar trends have been noted in spatially developing, buoyancy-driven bubbly flows (e.g. Ruiz-Rus *et al.* 2022), but the present results arise in a spatially decaying, very-high-Reynolds-number turbulent flow, where coalescence likewise produces distributions biased toward larger bubbles, consistent with observations in fully developed horizontal pipe flows (Razzaque *et al.* 2003*b*) and in decaying turbulence (Serizawa *et al.* 1975). Our findings here similarly indicate that in the axial direction, the turbulence-decaying, coalescence-dominated regime yields a lower peak and broader $f(d)$ distribution.

Higher ϕ leads to a broader and flatter bubble size distribution as shown in figure 8 ($a \rightarrow d$, $b \rightarrow e$, $c \rightarrow f$), with an enhanced probability of larger bubbles. In these higher void fraction cases, the distribution's large-diameter tail becomes more pronounced, meaning a greater presence of big bubbles compared with lower void conditions. The physics driving this trend is the increased frequency of bubble–bubble collisions at higher ϕ. Even though the flow is turbulent, a higher collision rate allows many small bubbles to merge into larger ones and decaying turbulence provides stability. Although rapidly decaying, developing turbulent multiphase flows are scarcely examined, our observations align with results for fully developed, coalescence-prone turbulence: increasing the void fraction ϕ raises the mean bubble size and broadens the distribution (Lehr *et al.* 2002). At high ϕ, collision probabilities, and hence, collision/coalescence frequencies, increase (Prince & Blanch 1990; Razzaque *et al.* 2003*b*), directly shaping the size–distribution function $f(d)$. By contrast, in strongly breakup-dominated regimes, bubble size can remain nearly independent of ϕ up to a threshold. In our measurements, coalescence plays a measurable role: as ϕ increases, enhanced bubble–bubble interactions shift $f(d)$ toward larger diameters and yield a broader, right-sided distribution, consistent with Lance & Bataille (1991).

While mean diameters and distribution widths characterise bulk bubble evolution, the probability density function (PDF) of sizes captures the complete statistical structure of the population. The PDF provides physical characterisation of the distribution: the presence and slope of power-law tails and their axial evolution – identify the dominant mechanism (inertial/capillary breakup versus coalescence) and delineate regime transitions (Deane & Stokes 2002; Chan *et al.* 2018). Figure 9 compares the bubble size PDF measured near the duct centreline at two axial locations ($\mathcal{L} = 3.6$ and 40) for two void fractions ($\phi = 0.5\,\%$ and $2\,\%$) and varying bulk velocities (or Q). Near the inlet ($\mathcal{L} = 3.6$), both void fraction cases (figures 9*a* and 9*c*) exhibit a similar dual-slope PDF behaviour on log–log plots. Bubble diameters in sub-Hinze follow an approximate $d^{-3/2}$ power law, indicating a no active breakup regime (mostly coalescence) (Crialesi-Esposito, Chibbaro & Brandt 2023). In this region ($\mathcal{L} = 3.6$ for all ϕ and V) virtually all of the bubble population lies under the Hinze diameter ($d/d_H < 1$), so turbulent eddies are too weak to overcome surface tension and break the bubbles. Consistently, breakup is relatively small at $\mathcal{L} = 3.6$ but bubble growth is governed by both coalescence and breakup. The observed $-3/2$ scaling is consistent with prior findings by Deane & Stokes (2002) in flows lacking active fragmentation, where this exponent is classically associated with sub-Hinze bubble generation via capillary mechanisms observed in breaking waves or turbulent-induced pinch-off events (Deane & Stokes 2002). For example, oceanic wave-breaking experiments showed that sub-Hinze bubbles obey a $d^{-3/2}$ size spectrum, similar to our inlet measurements (Deane & Stokes 2002; Farsoiya *et al.* 2023; Roccon, Zonta & Soldati 2023; Jain & Elnahhas 2025). This finding also accords with the notion that as long as bubbles remain smaller than the critical Hinze size for breakup, successive collisions

https://doi.org/10.1017/jfm.2026.11410 Published online by Cambridge University Press

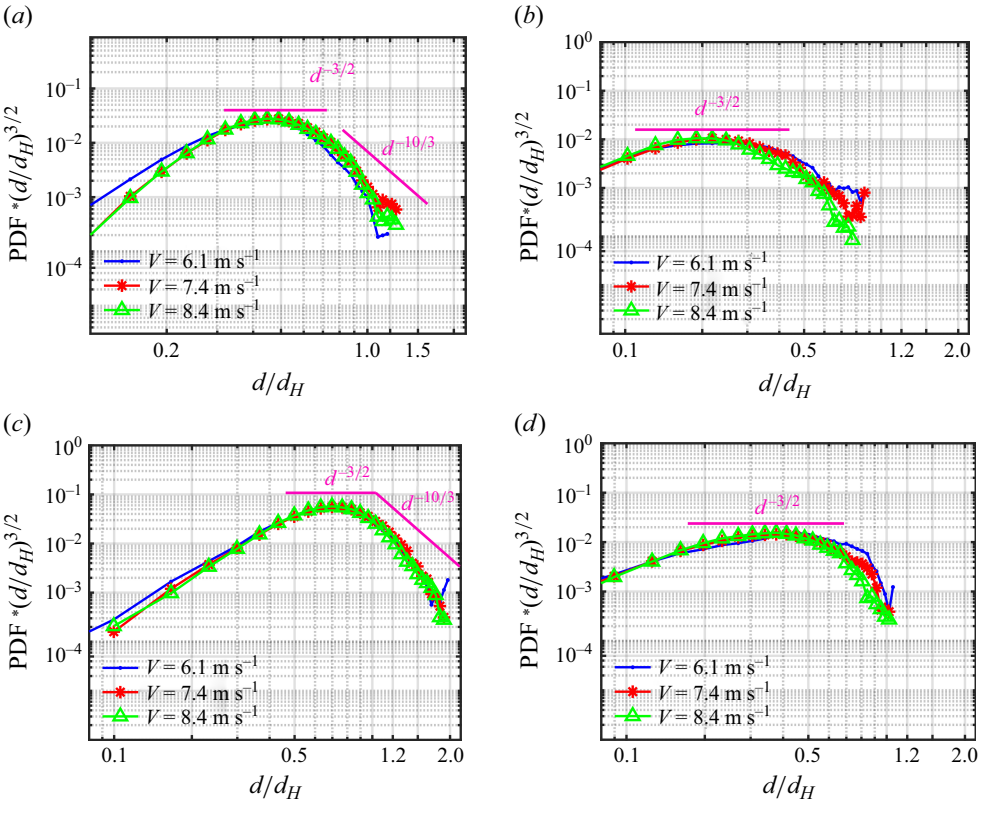


Figure 9. Scaling of compensated probability density function (PDF$*(d/d_H)^{(3/2)}$). The bubble size (d) is normalised with the Hinze scale (d_H). Sub-Hinze power-law scaling: $d^{-3/2}$; Super-Hinze power-law scaling: $d^{-10/3}$. (a) PDF near centre ($\mathcal{L} = 3.6$) at $\phi = 0.5\,\%$, (b) PDF near centre ($\mathcal{L} = 40$) at $\phi = 0.5\,\%$, (c) PDF near centre ($\mathcal{L} = 3.6$) at $\phi = 2\,\%$, (d) PDF near centre ($\mathcal{L} = 40$) at $\phi = 2\,\%$.

will merge them into larger bubbles and broaden the distribution without any competing fragmenting mechanism (Guo *et al.* 2016). Our data indeed provide direct evidence of such a coalescence-driven cascade: an initially narrow bubble size distribution at the duct inlet rapidly evolves into a broader $d^{-3/2}$ distribution before any significant breakup occurs. Notably, this near inlet $d^{-3/2}$ PDF holds for all tested flow conditions – all three liquid velocities and both void fractions collapse to the same slope at $\mathcal{L} = 3.6$ – underscoring that the early developing flow is a robust coalescence-dominated regime largely independent of ϕ or $\mathcal{I}$ (Prince & Blanch 1990; Farsoiya *et al.* 2023). Although most of the bubbles are sub-Hinze scale, there are considerable amounts of bubbles with super-Hinze scale ($d > d_H$) at $\mathcal{L} = 3.6$ due to still high ε. These super-Hinze scale bubbles are susceptible to turbulent breakup, causing the PDF's upper tail to steepen toward a $\sim d^{-10/3}$ slope. Figure 9 shows that once bubbles exceed the local d_H, they indeed begin to fragment and the distribution tail assumes the characteristic $\sim d^{-10/3}$ form associated with inertial breakup. This $d^{-10/3}$ scaling for fragmenting bubbles is consistent with classical fragmentation cascade models (Garrett & Li 2000) and has been observed in experiments and simulations of turbulent dispersions (Soligo, Roccon & Soldati 2019). Near the tail of figure 9(a,c), the distributions for $d/d_H > 1$ at $\mathcal{L} = 3.6$ exhibit slopes steeper than $-10/3$, ranging from -3.8 to -4.5, i.e. close to but slightly steeper than the inertial-breakup scaling. Owing to

https://doi.org/10.1017/jfm.2026.11410 Published online by Cambridge University Press

the low void fraction, the occurrence of large bubbles is sparse, which can make the tail appear artificially steep, consistent with the trend reported by Farsoiya *et al.* (2023).

Far downstream ($\mathcal{L} = 40$), the bubble size distribution has shifted and developed a pronounced single-slope scaling. All bubbles remain sub-Hinze and continue to follow the coalescence-dominated $d^{-3/2}$ trend. Unlike an equilibrium regime where breakup balances coalescence effects, here coalescence still dominates the majority of the duct region, while limited breakup occurs only near the inlet ($\mathcal{L} < 5{-}8$, depending on V) where ε is very high. In fact, beyond the $\mathcal{L} > 5{-}8$ downstream of the inlet, turbulent energy has decayed so substantially that super-Hinze scale bubble breakup becomes non-existent – the flow effectively transitions into a nearly purely coalescence-driven regime. The disappearance of the super-Hinze tail with increasing $\mathcal{L}$ (from $\mathcal{L} = 3.6$) indicates that while some bubbles briefly exceed the Hinze scale, they are rapidly broken up, preventing a persistent super-Hinze population. This behaviour is fully consistent with the concept of the Hinze scale acting as a cutoff: a critical diameter d_H exists at which turbulent dynamic pressure balances capillary pressure ($\rho \mathcal{V}^2 \sim \gamma / d_H$), corresponding to a Weber number of order unity ($We \sim \mathcal{O}(1)$) for breakup onset (Hinze 1955). This equilibrium size concept has long been utilised in population-balance models to predict stable bubble size distributions in steady-state bubbly flows (Lehr *et al.* 2002). In our decaying flow, however, the continuous reduction in turbulence intensity with increasing $\mathcal{L}$ ensures that bubbles rarely exceed the Hinze scale. Bubbles that do exceed the Hinze scale are not actively fragmented. Consequently, beyond a few hydraulic diameters from the inlet, bubble coalescence mostly proceeds unopposed by breakup.

The influences of ϕ and V on the PDF scaling trends are also evident in figure 9. Near the inlet ($\mathcal{L} \leq 8.2$), cases with a higher void fraction ($\phi = 2\,\%$ vs $0.5\,\%$) exhibit a broader distribution due to accelerated coalescence-driven bubble growth, along with a more pronounced tail of large bubbles following the $d^{-10/3}$ scaling (comparing figures 9*c* and 9*a*). Although at $\mathcal{L} = 40$, the $2\,\%$ case exhibits predominantly a single-slope regime, it still displays a longer large bubble tail compared with the $0.5\,\%$ case – again attributable to the enhanced coalescence at higher ϕ (comparing figures 9*d* and 9*b*). This trend aligns with theoretical expectations: a higher concentration of bubbles increases the frequency of collisions and consequently the coalescence rate, allowing bubbles to reach the critical Hinze scale more rapidly (Guo *et al.* 2016). In practical terms, increasing the void fraction enhances the extent of the distribution and leads to an earlier formation of large, unstable bubbles susceptible to breakup within a few hydraulic diameters from the inlet – manifesting as an extended $d^{-10/3}$ fragmentation tail. Downstream of this region, even as the turbulence continues to decay, the higher ϕ case maintains a larger population of bubbles and a longer $d^{-3/2}$ tail relative to the lower ϕ case.

Bulk liquid velocity exerts a subtler yet important influence on the PDF scaling. Remarkably, for a given void fraction ϕ, the normalised distributions, plotted as PDF vs d/d_H, collapse onto one another, showing strong overlap across different axial locations $\mathcal{L}$ and velocities V. This collapse suggests a self-similar evolution of the bubble size distribution when scaled by the local Hinze diameter. The behaviour can be understood by examining the role of ε: higher liquid velocities inject more turbulent energy, leading to greater dissipation rates (ε) and consequently smaller Hinze scales (d_H). In these high-V cases, strong turbulence suppresses the coalescence-driven growth (due to reduced coalescence time scales) of large bubbles by fragmenting them early, effectively 'nipping in the bud' any transition toward a broader distribution (Prince & Blanch 1990). As a result, the bubble population in high-V flows remains narrowly distributed and biased toward smaller diameters, with minimal spread around the mean. Conversely, lower velocity flows (e.g. $V = 6.1\ \mathrm{m\ s^{-1}}$) exhibit weaker turbulence (smaller ε) and, thus, larger Hinze diameters

https://doi.org/10.1017/jfm.2026.11410 Published online by Cambridge University Press

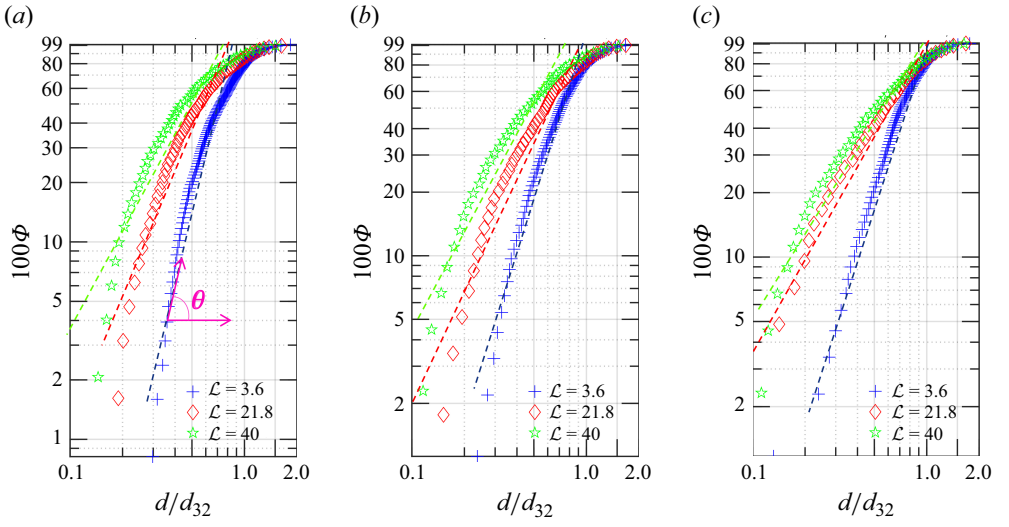


Figure 10. Cumulative bubble size distribution (Φ) with bubble size (d/d_{32}) at $V = 6.1\,\mathrm{m\,s^{-1}}$. The slopes $\theta(\mathcal{L}_1, \mathcal{L}_2, \mathcal{L}_3)$ are reported at three axial locations, where $\mathcal{L}_1 = 3.6$, $\mathcal{L}_2 = 21.8$ and $\mathcal{L}_3 = 40$. Here σ_g is calculated using (4.7). Results are shown for (*a*) $\phi = 0.5\,\%$, $\theta \in$ (3.63,2.11,1.59), and $\sigma_g \in$ (1.48,1.76,1.91); (*b*) $\phi = 1\,\%$, $\theta \in$ (2.61,1.76,1.55), and $\sigma_g \in$ (1.54,1.84,1.96); (*c*) $\phi = 2\,\%$, $\theta \in$ (2.52,1.45,1.39), and $\sigma_g \in$ (1.57,1.89,2.03).

(Yang *et al.* 2025). Under such conditions, bubbles can grow to larger sizes before turbulent stresses are sufficient to induce breakup, resulting in a broader size distribution and a more prominent large bubble population. Although the low-V flows still experience decaying turbulence and correspondingly smaller d_H farther downstream, the diminished fragmentation enables broader coalescence-driven growth. These results confirm that the bubble size distribution in decaying turbulent flows scales robustly with the local Hinze diameter, and the PDFs exhibit a self-similar trend across a range of flow conditions.

The cumulative bubble size distribution Φ, plotted as a function of the normalised diameter d/d_{32}, provides a compact description of the evolving bubble population in the decaying turbulent flow (Razzaque *et al.* 2003*b*). Figure 10 shows Φ at $V = 6.1\,\mathrm{m\,s^{-1}}$ for $\phi = 0.5\,\%,\ 1\,\%,\ 2\,\%$, comparing measurements at $\mathcal{L} = 3.6,\ 21.8$ and 40. For each case, we report a fitted slope (θ), together with the σ_g, which directly characterises the width of the corresponding log-normal distribution. At $\phi = 0.5\,\%$, the distribution near the inlet ($\mathcal{L} = 3.6$) is relatively steep ($\theta = 3.63$), whereas downstream the curves flatten ($\theta = 2.11$ at $\mathcal{L} = 21.8$ and $\theta = 1.59$ at $\mathcal{L} = 40$). Consistently, σ_g increases from 1.48 to 1.91 with $\mathcal{L}$, indicating progressive broadening of the distribution as the flow convects downstream. These trends are consistent with earlier pipe flow studies (Hesketh *et al.* 1987; Razzaque *et al.* 2003*b*). Hesketh *et al.* (1987) showed that, in breakup-dominated conditions, the distribution approaches a self-preserving log-normal form with nearly invariant width ($\sigma_g \approx 1.2$–1.4). In contrast, Razzaque *et al.* (2003*b*) demonstrated that, under coalescence-dominated conditions, the distribution broadens downstream, with σ_g typically increasing to $\approx$1.7–2.0. Thus, the distribution width is not universal, but reflects the local competition between breakup and coalescence. For $\phi = 0.5\,\%$ at $\mathcal{L} = 3.6$, $\sigma_g \approx 1.48$, reflecting a slight widening beyond the canonical breakup range. This is consistent with the fact that the strongest turbulent fragmentation occurs within the pump, whereas measurements are taken in the duct where turbulence has already decayed. The inlet region therefore retains significant breakup, but is no longer fully breakup dominated. As turbulence decays

https://doi.org/10.1017/jfm.2026.11410 Published online by Cambridge University Press

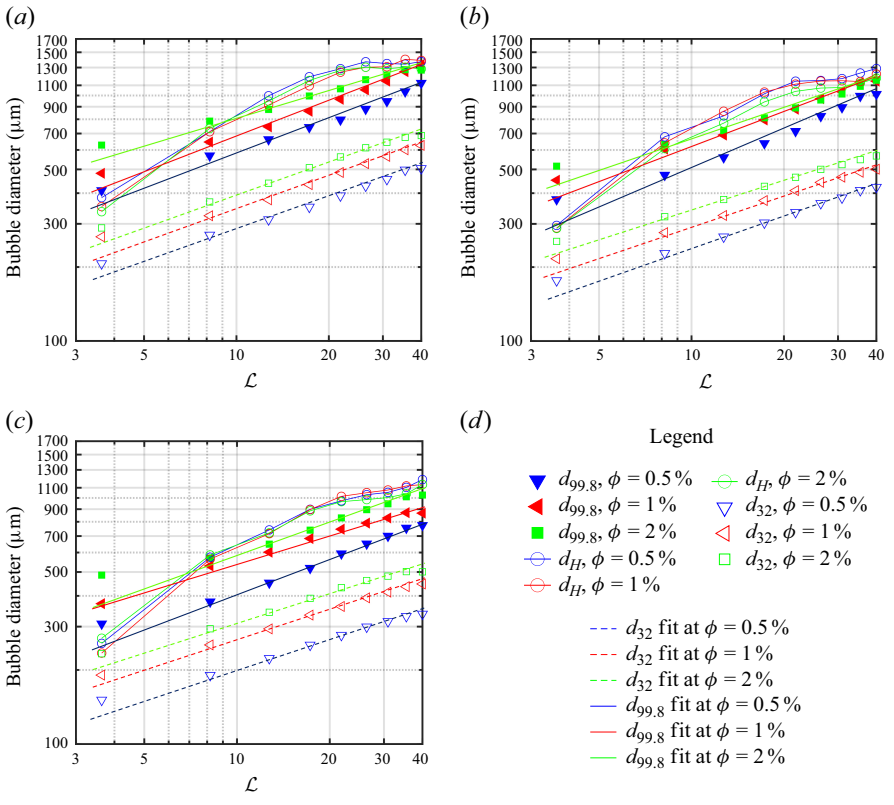


Figure 11. Axial variation of $d_{99.8}$, d_{32} and d_H in the developing turbulent duct flow. The reported fit parameters β_{exp} (power law coefficient) and R^2 (coefficient of determination) are obtained from data for $\mathcal{L} > 3.6$, excluding the first data point, and are reported in table 1. Results are shown for (*a*) $V = 6.1\,\mathrm{m\,s^{-1}}$, (*b*) $V = 7.4\,\mathrm{m\,s^{-1}}$, (*c*) $V = 8.4\,\mathrm{m\,s^{-1}}$, (*d*) the legend.

further downstream, breakup weakens, coalescence becomes increasingly effective and the distributions migrate into the coalescence-dominated range ($\sigma_g \gtrsim 1.7$), in agreement with observations that turbulence decay promotes bubble growth through coalescence (Chan *et al.* 2018; Chieco & Durian 2023). Increasing ϕ produces flatter cumulative curves (smaller θ) and larger σ_g. The stronger broadening at higher ϕ reflects enhanced collision frequency and coalescence probability. With increasing ϕ ($0.5\,\% \rightarrow 1\,\% \rightarrow 2\,\%$), σ_g approaches 1.7–2.0 faster, characteristic of strongly coalescence-dominated conditions, whereas lower void fractions require longer axial development to reach similar states.

The axial evolution of the bubble size distribution, combining d_{32} with high quantiles such as $d_{99.8}$ (99.8th percentile bubble diameter) and referencing the Hinze scale d_H, captures both bulk and tail dynamics as turbulence decays. Identifying shifts between breakup-limited and coalescence-dominated regimes is critical, since the former suppresses large bubbles while the latter promotes tail broadening and enhanced interfacial renewal. Regime-resolved distribution tracking therefore provides stringent calibration targets for population-balance models and a mechanistic basis for reliable scale-up.

Figure 11 presents the axial variation of bubble size statistics near the centre of the duct ($6 \times 6\,\mathrm{mm^2}$) on a log–log scale, namely d_{32}, $d_{99.8}$, and the Hinze scale d_H, for each void fraction ϕ and bulk velocity V. The Hinze scale is evaluated locally at each axial position using (1.1). As $\mathcal{L}$ increases, the Hinze scale d_H grows linearly on a log–log scale (following

https://doi.org/10.1017/jfm.2026.11410 Published online by Cambridge University Press

	β_{exp} (Experimental)						R^2					
Flow rate	ϕ_1		ϕ_2		ϕ_3		ϕ_1		ϕ_2		ϕ_3	
V (m s^{-1})	d_{32}	$d_{99.8}$	d_{32}	$d_{99.8}$	d_{32}	$d_{99.8}$	d_{32}	$d_{99.8}$	d_{32}	$d_{99.8}$	d_{32}	$d_{99.8}$
6.1	0.45	0.48	0.49	0.48	0.46	0.46	0.97	0.96	0.98	0.96	0.98	0.94
7.4	0.46	0.49	0.47	0.46	0.45	0.44	0.97	0.92	0.98	0.96	0.99	0.94
8.4	0.46	0.53	0.45	0.47	0.47	0.50	0.99	0.95	0.98	0.95	0.98	0.94

Table 1. Power-law coefficient (β_{exp}) and coefficient of determination (R^2) for the fits for the axial variation of $d_{99.8}$, d_{32} and d_H shown in figure 11.

the power law). Downstream, the dissipation ε decreases markedly (by approximately 90 % over the test section; see figure 7). Through (1.1), this gives $d_H \propto \varepsilon^{-2/5}$, so a rapid fall in ε produces only a gradual increase in d_H. If $\varepsilon \sim \mathcal{L}^{-m}$ with $m \approx 1.85$ to 2.2 (see figure 7), then $d_H \sim \mathcal{L}^{2m/5}$, that is, $d_H \sim \mathcal{L}^{0.74}$ to $\mathcal{L}^{0.88}$. Thus, the growth of d_H with $\mathcal{L}$ becomes sublinear on the log–log scale.

In comparison, $d_{99.8}$ also grows linearly (on log–log; general power law) with a smaller slope along the axial direction and remains below d_H at all axial locations except near the inlet ($\mathcal{L} \approx 3.6$). Near the inlet, the size distribution straddles the Hinze scale, so bubbles exist on both sides of d_H; those with $d > d_H$ are susceptible to turbulence-induced breakup. Downstream, as turbulence decays, d_H increases faster than $d_{99.8}$, so $d_{99.8}$ falls below and stays below d_H. After $\mathcal{L} > 8.2$, roughly no bubbles exceed d_H, which indicates a coalescence–dominated regime with active breakup effectively suppressed. The d_{32} also shows a power-law growth (linear on log–log) with $\mathcal{L}$ (except near the inlet), but it remains well below both $d_{99.8}$ and d_H. The monotonic rise of d_{32} is consistent with coalescence-driven growth.

For $\mathcal{L} \geq 8.2$, both $d_{99.8}$ and d_{32} follow power-law trends with $\mathcal{L}$ in figure 11, and the corresponding fit parameters are listed in table 1. The fits are strong, with R^2 values close to 0.95. The fitted exponents β_{exp} lie within 0.45 to 0.51, indicating that the mean and the upper-tail bubble sizes increase at comparable rates in the coalescence-dominated regime. The theoretical scaling for the growth of d_{32} and $d_{99.8}$ follows from the effective coalescence rate Γ, defined as the product of the collision frequency h and the coalescence efficiency λ (Coulaloglou & Tavlarides 1977; Prince & Blanch 1990):

$$\Gamma = h\,\lambda. \tag{4.8}$$

Classical inertial-range scaling (Kolmogorov 1991), as presented in standard treatments (Batchelor 1953; Monin & Yaglom 2013), underpins collision models for bubbly dispersions. In these measurements, bubble interactions are driven by inertial-subrange eddies, consistent with the observed length-scale ordering $\eta \ll d \sim \lambda_T \ll \ell$, for which $d/\eta \gg 1$ and $d/\lambda_T = \mathcal{O}(1)$. In the inertial subrange of turbulence, the velocity increment u_{rel} across a bubble scale d follows Kolmogorov similarity, resulting in (Batchelor 1953; Monin & Yaglom 2013)

$$u_{rel}(d) \sim (\varepsilon d)^{1/3}, \tag{4.9}$$

where ε is the mean turbulent dissipation rate. The relative-velocity scaling is based on interactions between bubbles and inertial-range eddies of comparable size. Accordingly, the collision velocity is governed by the turbulent velocity difference evaluated at the inter-bubble separation scale (Coulaloglou & Tavlarides 1977; Prince & Blanch 1990; Luo & Svendsen 1996; Kamp *et al.* 2001). Combining the inertial–range relative velocity with the

https://doi.org/10.1017/jfm.2026.11410 Published online by Cambridge University Press

geometric cross-section $\sim d^2$ yields the turbulent collision kernel

$$h \propto u_{rel}(d) \times d^2 \propto \varepsilon^{1/3}\, d^{7/3}. \tag{4.10}$$

As shown in Appendix C, the assumption of spherical bubbles is justified because the bubble interfacial relaxation time is comparable to or shorter than the integral-scale eddy turnover time, allowing the interface to re-equilibrate between successive collisions (Kumar *et al.* 2026). Further simplification results in

$$\Gamma = 8C\,\lambda\,(\varepsilon)^{1/3}\, d^{\frac{7}{3}}. \tag{4.11}$$

The kernel has units of volume per unit time and the coalescence efficiency satisfies $\lambda \in [0, 1]$. The evolution of the number density n can then be expressed using Smoluchowski's binary coagulation equation (accounting for double counting and assuming a monodisperse distribution) (Kreer & Penrose 1994):

$$\frac{\mathrm{d}n}{\mathrm{d}t} = -\frac{1}{2}\,\Gamma\, n^2. \tag{4.12}$$

The rationale for this monodisperse simplification is that, in the present high-turbulence regime, both collisions and successful coalescence are dominated by similar-sized bubbles, with the coalescence efficiency highest when bubble sizes are comparable, leading to a kernel that is sharply peaked near unity size ratios (Liao & Lucas 2010; Tan *et al.* 2025). For duct flow, substituting $t = \mathcal{L}/\mathcal{V}$ and $n = 6\phi/(\pi d^3)$ into (4.12), and simplifying for decaying turbulence with $\varepsilon = \varepsilon(\mathcal{L})$ (refer Appendix C), we obtain

$$\frac{\mathrm{d}d}{\mathrm{d}\mathcal{L}} \equiv K_o[\varepsilon(\mathcal{L})]^{1/3} d^{\frac{1}{3}}, \tag{4.13}$$

where K_o depends on λ. Under the present flow conditions, λ is evaluated using the commonly employed film drainage model and is found to be a constant (see Appendix C). Using a power-law decay referenced to a finite start location $\mathcal{L} > 0$ (see (4.5)):

$$d(\mathcal{L}) \propto \mathcal{L}^{\frac{3-m}{2}} \propto \mathcal{L}^{\beta_{th}}, \quad \text{where} \quad \beta_{th} = \frac{3-m}{2}. \tag{4.14}$$

The theoretical power-law coefficient β_{th} in (4.14) is listed in table 2. For m in the range 1.85–2.10, β_{th} varies from 0.45 to 0.57, which closely matches the experimentally fitted exponents for d_{32} and $d_{99.8}$, from 0.44 to 0.53, in table 1. Thus, a steeper dissipation decay (larger m) corresponds to a larger β_{th}. At fixed m, higher sustained ε increases the collision frequency and accelerates bubble size growth. For applications that require tight control of the size distribution (for example, targeting d_{32} or $d_{99.8}$), one may adjust m by passive means such as modifying wall conditions or by active means such as acoustic or ultrasonic forcing. To make d grow in parallel with the Hinze scale, one could equate the scalings $d \sim \mathcal{L}^{(3-m)/2}$ and $d_H \sim \mathcal{L}^{2m/5}$, which gives $m = 5/3$. At $m = 5/3$, both d_{32} and $d_{99.8}$ remain self-similar and grow in parallel with d_H as $\mathcal{L}$ increases.

Near the inlet, the pure-coalescence scaling does not apply because breakup remains active. Figure 11 shows that, owing to breakup and an initially unstable distribution, $d_{99.8}$ is capped and grows at a different rate than d_{32}; consequently, the ratio $\mathcal{D} = d_{99.8}/d_{32}$ evolves through the entry region before saturating downstream (once the two growth curves become roughly parallel). Consistent with this behaviour, Razzaque *et al.* (2003*b*) reported that monodisperse injections ($\mathcal{D} \approx 1$) in fully developed, coalescence-dominated turbulence relax to a constant $\mathcal{D} \approx 2.2$. Monitoring $\mathcal{D}$ is operationally important in mixing, heat-transfer and reactor applications because it governs interfacial area and distribution shape (Lehr *et al.* 2002; Risso 2018).

https://doi.org/10.1017/jfm.2026.11410 Published online by Cambridge University Press

ε scaling	$d(d_{32}$ and $d_{99.8})$ scaling
$\varepsilon \propto \mathcal{L}^{-m}$	$d \propto \mathcal{L}^{\beta_{th}}$
$\varepsilon \propto \mathcal{L}^{-1.85}$	$d \propto \mathcal{L}^{23/40}$
$\varepsilon \propto \mathcal{L}^{-2}$	$d \propto \mathcal{L}^{1/2}$
$\varepsilon \propto \mathcal{L}^{-2.1}$	$d \propto \mathcal{L}^{9/20}$

Table 2. Bubble diameter scaling in highly decaying turbulent flow. Here $\beta_{th} = 3 - m/2$.

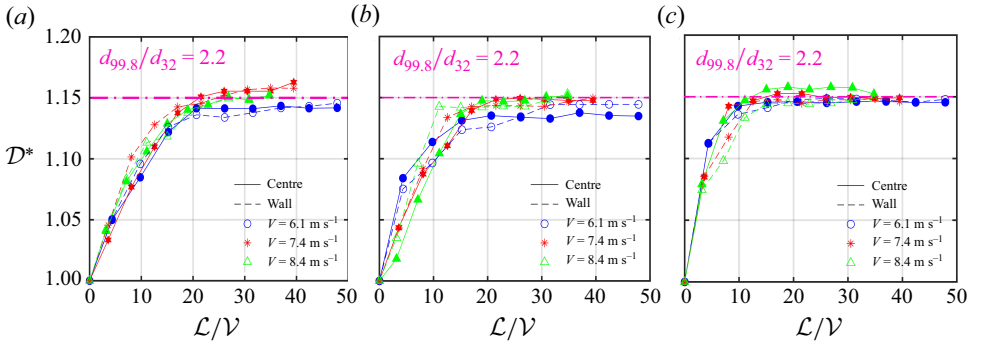


Figure 12. Variation of $\mathcal{D}^*$(normalised) in a developing turbulent duct flow. Results are shown for (*a*) $\phi = 0.5\,\%$, (*b*) $\phi = 1\,\%$, (*c*) $\phi = 2\,\%$.

The axial evolution of $\mathcal{D}$ quantifies tail heaviness relative to the interfacial-area–weighted mean, providing a robust, outlier-resistant proxy for the largest statistically reliable bubbles (preferable to raw $d_{\max}$) and for population broadening as turbulence decays (Razzaque *et al.* 2003*a*; Risso & Fabre 1998). Figure 12 presents the streamwise evolution of the normalised bubble size ratio $\mathcal{D}^*$ (normalised by $\mathcal{D}_o$, which is $\mathcal{D}$ at $\mathcal{L} = 0$) for three ϕ at three V. The initial $\mathcal{D}_o$ ($\approx 1.91 \pm 0.02$) is nearly invariant across ϕ and V because intense inlet turbulence rapidly breaks larger bubbles and promotes the swift coalescence of smaller ones, yielding a narrow distribution. The figure shows $\mathcal{D}^*$ is virtually the same at the duct centre and near the wall (differences $<5\,\%$), indicating that the bubble size distribution width is almost uniform across the cross-section. This is consistent with the expectation that in a fully developed (dynamic equilibrium) bubbly flow, the size distribution becomes independent of position (Kleinstreuer & Agarwal 2001). Across all the variables, $\mathcal{D}^*$ stays within a range of approximately 1–1.15. In the developing region (near the inlet), $\mathcal{D}^*$ rises with axial distance $\mathcal{L}$, reflecting the broadening of the bubble size distribution due to coalescence. Higher void fractions (1 % and 2 %) reach this plateau earlier (at smaller t), whereas at 0.5 % the ratio requires a longer time to level off. This trend indicates a coalescence-dominated flow development – as bubbles travel downstream, frequent coalescence creates larger bubbles and a wider size spread until a balance is achieved. The eventual 'saturation' value of $\mathcal{D}^*$ falls around 1.15 (where $\mathcal{D} \approx 2.2$) for all velocity and void fraction combinations (with the caveat that the 0.5 % case may not have fully reached its plateau in the available length). Once this value is attained, the distribution width no longer grows with $\mathcal{L}$, implying that breakup and coalescence rates have equilibrated.

The observed plateau ratio of $\mathcal{D}^* \approx 1.15$ ($\mathcal{D} \approx 2.2$) is consistent with the results of Razzaque *et al.* (2003*b*) for fully developed turbulent flow fields dominated by coalescence. The value $\mathcal{D}_o \approx 1.9$ is characteristic of a breakup-controlled regime: Evans,

https://doi.org/10.1017/jfm.2026.11410 Published online by Cambridge University Press

Jameson & Atkinson (1992) reported $\mathcal{D} \approx 1.8$ in liquid-jet bubble columns where turbulent breakup primarily set the bubble sizes. The initial slightly larger value reflects the short delay between bubble formation (due to breakup) in the pump and the first viewing station, during which limited decay and early coalescence shift the upper tail upward. Thus, the inlet condition sampled here corresponds to a near-breakup-controlled distribution, from which the flow subsequently evolves into a coalescence-dominated regime downstream. Notably, Razzaque *et al.* (2003*b*) also found that in the coalescence-dominated regime this ratio becomes nearly independent of axial position, bulk velocity and void fraction, mirroring our observation that once the distribution equilibrates, further axial evolution of $\mathcal{D}^*$ is weak. Prince & Blanch (1990)'s classic bubble-column experiments, together with their population-balance model, showed that beyond a certain column height (the 'dynamic equilibrium region') the bubble size distribution becomes independent of axial position and reflects a self-preserving distribution, and Lehr *et al.* (2002) consistently demonstrated in simulations that once coalescence and breakup reach balance, the distribution shape no longer evolves with height. In summary, the plateau in $\mathcal{D}^*$ marks the attainment of a self-preserving bubble size distribution: the overall shape no longer evolves with $\mathcal{L}$, even though individual bubbles continue to merge and break. The common asymptotic value of $\mathcal{D} \approx 2.2$ reported in the literature therefore serves as a practical reference for identifying equilibrium conditions and for evaluating breakup–coalescence models.

The exponential broadening of the size ratio arises from several coalescence mechanisms acting together. Random turbulent fluctuations in the liquid velocity field induce stochastic bubble–bubble encounters and bring bubbles from different streamlines into contact, increasing the collision frequency beyond laminar drift (Prince & Blanch 1990). In our high-*Re* flow, the random bubble–bubble encounters are overwhelmingly driven by the strong background turbulence; estimates of the bubblance parameter ($b \approx 10^{-5}$–10^{-3}, ratio of bubble-induced turbulence to background turbulence) and the associated time scales confirm that the bubble-induced agitation is negligible by comparison. Turbulence-induced coalescence has therefore been modelled as a dominant mechanism in similar systems (Kamp *et al.* 2001; Bröder & Sommerfeld 2004). A second contribution arises from velocity shear and differential buoyancy. Faster-rising bubbles overtake slower ones, and velocity gradients near the wall promote collisions, consistent with Prince and Blanch's identification of turbulence, buoyancy-induced velocity differences, and laminar shear as primary collision sources (Prince & Blanch 1990). All three are relevant here: even in co-current flow, larger bubbles have higher rise velocities relative to the liquid and can catch up to smaller ones (a buoyancy-driven overtaking collision), while shear in the liquid especially near walls creates lateral motion that brings bubbles into contact. Third, radial migration redistributes bubbles in a way that further enhances coalescence. Small nearly spherical bubbles tend to move toward the wall, whereas larger deformable bubbles migrate toward the centreline (Lucas, Beyer & Szalinski 2023). As bubbles grow, they accumulate in the core where collision frequency increases, while smaller bubbles remain near the periphery with fewer encounters. Wake entrainment behind large bubbles further increases collision likelihood (Ruiz-Rus *et al.* 2022). The resulting radial structure reflects turbulent dispersion, shear-induced collisions, lateral lift-induced migration, wake entrainment and differential buoyancy effects (negligible here) (Tomiyama 1998; Tomiyama *et al.* 2002). In flows containing small bubbles and very high carrier-flow turbulence, bubble–bubble collisions are dominated by the carrier turbulence by more than an order of magnitude, whereas bubble-induced turbulence, shear, buoyancy-driven motion, lift-induced migration and wake capture primarily act to redistribute bubbles rather than generate additional collisions

https://doi.org/10.1017/jfm.2026.11410 Published online by Cambridge University Press

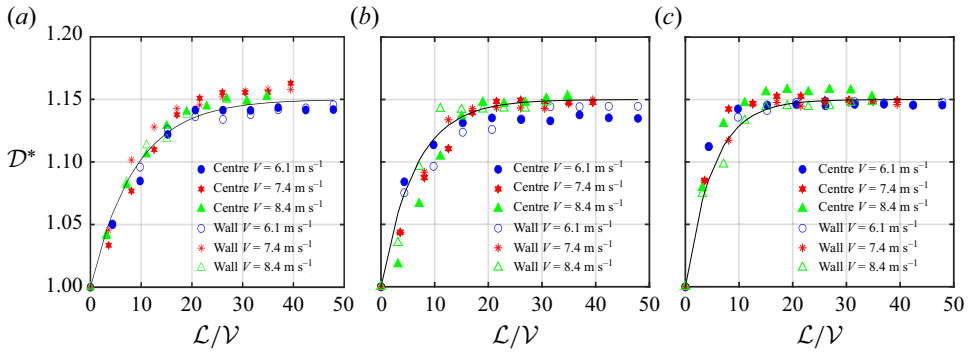


Figure 13. Transient variation of $(\mathcal{D})^*$(curve fitted) in a developing turbulent duct flow. Results are shown for (*a*) $\phi = 0.5\,\%$, (*b*) $\phi = 1\,\%$, (*c*) $\phi = 2\,\%$.

(Lance & Bataille 1991; Prakash *et al.* 2016; Alméras *et al.* 2017; van den Berg *et al.* 2020). Together, these mechanisms produce an initial burst of coalescence when many small bubbles are present, followed by slower coalescence as the bubble number decreases and the distribution approaches equilibrium.

As discussed, the $\mathcal{D}^*$ increases monotonically with $\mathcal{L}$. Empirically, the evolution follows an exponential relaxation towards an asymptote as seen in figure 13 and fitted with

$$\mathcal{D}^* = 1.15 - 0.15\mathrm{e}^{-\frac{t}{\tau}}; \quad \text{where} \quad \mathcal{D}^* = \frac{\mathcal{D}}{\mathcal{D}_o}, \tag{4.15}$$

$$\Delta\mathcal{D}^*(\,\%) = \frac{\mathcal{D}^*_{max} - \mathcal{D}^*}{\mathcal{D}^*_{max}} \times 100 \approx 13\,\mathrm{e}^{-\frac{t}{\tau}}, \tag{4.16}$$

where τ is a characteristic relaxation time. Near the duct inlet at $\mathcal{L} = 0$, $\mathcal{D}^* = 1$ by definition; downstream it rises toward an asymptotic value of 1.15 (a 15 % increase). This exponential trend indicates a first-order process: the rate of change of the size ratio is highest near the inlet (where the distribution is narrow) and decays progressively as the distribution broadens and approaches a new equilibrium state. Such behaviour is consistent with classical coagulation kinetics, wherein the population's evolution can be characterised by a single dominant time scale (Ruiz-Rus *et al.* 2022). The form of the above relation is analogous to Smoluchowski's theory for Brownian coalescence (with τ playing the role of a 'half-life' of the initial population) (Ruiz-Rus *et al.* 2022).

Figure 13 shows that the axial evolution of the normalised diameter ratio, $\mathcal{D}^*$, as a function of residence time (t), demonstrates a universal trend. Symbols represent experimental data measured at different bulk velocities ($V = 6.1$–8.4 m s^{-1}) and radial positions (centreline and near-wall) for initial void fractions of $\phi = 0.5\,\%$, $1\,\%$ and $2\,\%$ in figure 13. The curve in each panel is the best-fit exponential (4.15), illustrating the rapid rise from unity at $t = 0$ toward an asymptote of about 1.15. A higher void fraction yields a steeper rise (smaller τ), consistent with more frequent bubble coalescence at larger ϕ. The $\mathcal{D}^*$ plotted versus time t, for all V measurements, near-wall and centreline, collapse onto a single normalised curve at fixed initial ϕ (see figure 13), implying a degree of universality in the coalescence dynamics. The evolution of $\mathcal{D}^*$ is therefore controlled primarily by ϕ and t, and is effectively independent of radial position. The influence of different bulk velocities is absorbed by the t scaling – faster flows simply convect bubbles further in a given time, but the coalescence progression per unit time is unchanged. Such behaviour suggests that the coalescence process is governed by the cumulative interaction time between bubbles, and that our normalisation captures the essential time scale of those

https://doi.org/10.1017/jfm.2026.11410 Published online by Cambridge University Press

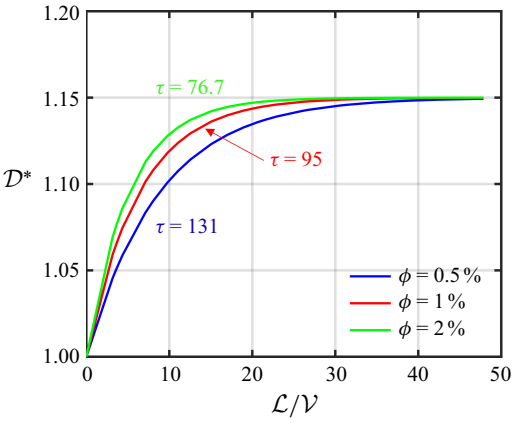


Figure 14. Transient variation of $\mathcal{D}^*$ and its deviation from equilibrium with residence time.

interactions. In our data, the master curve is well described by the above exponential fit, reinforcing the notion that a first-order kinetics governs the axial broadening of the bubble size distribution.

Each master curve is, however, parameterised by the initial void fraction ϕ. The relaxation length (or e-folding length) τ in the exponential fit depends strongly on ϕ, whereas other parameters (e.g. bulk velocity, radial position) have negligible influence on τ. Quantitatively, increasing ϕ from 0.5 % to 2 % reduces τ from 131 to 76.7 (as inferred from the curves in figure 14), indicating that bubble populations with more initially crowded conditions coalesce and relax to their new size distribution much sooner. This indicates that τ is essentially an increasing function of the initial bubble spacing (or inverse function of ϕ). Importantly, τ in our flow appears to be independent of the mean velocity V, consistent with the notion that, in the reference frame of the flow, the intrinsic coalescence time scale is set by bubble collision kinetics (dictated by ϕ and turbulence levels) rather than convective transport.

4.3. *Void fraction (ϕ)*

In order to explore the radial variation of the local void fraction, the observation window was divided into coloured regions (see figure 2*b*), corresponding to near-wall (red) and central (blue) zones. For each region, several hundred 2D images were analysed to extract the bubble size distribution, repeating until the results became statistically stationary. The local void fraction in each region was then determined as the volume-weighted mean bubble volume per image, normalised by the total region volume. The local void fraction is denoted by ϕ_{wall} for near-wall and ϕ_{centre} for centreline. While these averages are assumed uniform within each coloured zone, minor radial variations may exist (Bunner & Tryggvason 2002, 2003; Lu & Tryggvason 2006; Balachandar & Eaton 2010; Du Cluzeau, Bois & Toutant 2019).

Figure 15 shows the change in local void fraction $\Delta\phi = \phi_{centre/wall} - \phi_0/\phi_0$ at the centre and wall in the axial direction of the duct across three ϕ (0.5 %, 1 %, 2 %). At the inlet ($\mathcal{L} = 0$), the void fraction is nearly uniform, with both centreline and near-wall values equal to the cross-sectional average (input value). As the flow develops downstream, a distinct segregation emerges: the near-wall void fraction decreases steadily, while the centreline void fraction increases commensurately, indicating progressive bubble accumulation in the core. For the lowest ϕ of 0.5 %, this redistribution is gradual but substantial; by the end

https://doi.org/10.1017/jfm.2026.11410 Published online by Cambridge University Press

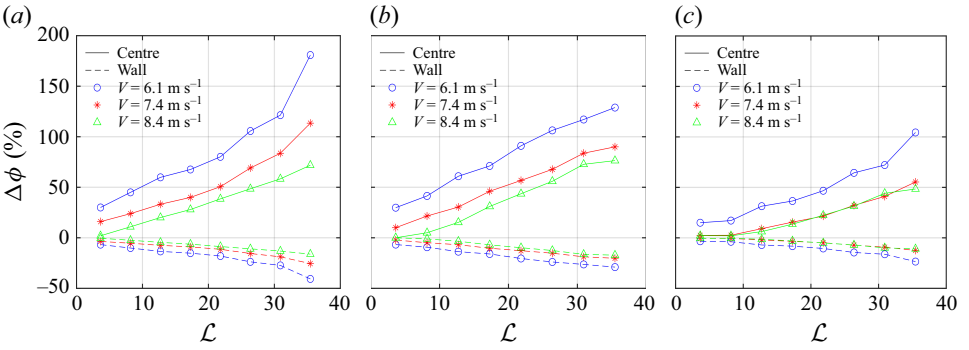


Figure 15. Variation of ϕ_{wall} and ϕ_{centre} with axial position ($\mathcal{L}$). Results are shown for (*a*) $\phi = 0.5\,\%$, (*b*) $\phi = 1\,\%$, (*c*) $\phi = 2\,\%$.

of the measured domain, the centreline void fraction rises to $\sim 1.6\times$ its inlet value, while the near-wall void fraction drops to $\sim 0.4\times$ its inlet value, resulting in a growing centre-wall void fraction difference ($\Delta\phi$) that increases nearly linearly with time and shows no plateau. At higher ϕ ($= 2\,\%$), a similar trend is observed with larger absolute changes: the centreline void fraction rises from 2 % to nearly 3 %, while the near-wall region is depleted to about 1 %. However, when normalised by the initial average, the relative enrichment at the core is slightly less pronounced at higher ϕ, indicating that bubble–bubble interactions and enhanced mixing at high void fractions can temper the relative segregation (Bunner & Tryggvason 2002, 2003; Burns *et al.* 2004*b*; Dabiri, Lu & Tryggvason 2013).

The influence of mean flow velocity is also evident. At lower bulk velocities ($V \approx 6.1\ \mathrm{m\,s^{-1}}$), the transition toward a core-peaked profile occurs more rapidly and distinctly, with bubbles segregating inward sooner and to a greater extent. At higher velocities ($V \approx 8.4\ \mathrm{m\,s^{-1}}$), void fraction profiles remain closer to uniform for longer axial distances and the centre-wall divergence grows more slowly. This arises because stronger turbulence at higher V is sustained farther downstream, keeping bubbles smaller and better mixed, and thus delaying the onset of segregation (Lu & Tryggvason 2006; Burns *et al.* 2004*b*; Balachandar & Eaton 2010). At lower V, turbulence decays more quickly, enabling earlier bubble coalescence and growth, which amplifies the effect of lift and buoyancy on radial migration (Bunner & Tryggvason 2003; Lu & Tryggvason 2006; Balachandar & Eaton 2010).

These observations represent a significant departure from classical duct/pipe flow studies, which consistently report wall-peaked void fraction profiles in turbulent flows (Delnoij *et al.* 1997; Hibiki & Ishii 1999). In these flows, small bubbles – owing to positive lift coefficients – accumulate near the wall, producing pronounced wall peaks. For our flow, however, even with small bubble sizes ($d_{32} \sim$ 200–600 μm), a strong and persistent core peak emerges. This divergence from established patterns indicates that bubble migration mechanisms in high Reynolds number, vertical bubbly flows are fundamentally distinct. A key novelty of the present study is the demonstration that core-peaking arises for bubbles an order of magnitude smaller than the classical lift-reversal diameter (typically 5–6 mm in air–water systems) (Tomiyama *et al.* 2002; Hidman *et al.* 2022). Traditional lift models predict that only sufficiently large, deformable bubbles undergo a reversal in the lateral lift force, driving them from the wall toward the core and generating centre-peaked profiles. Our experiments, however, show that even micron-scale bubbles experience strong inward migration under diminished turbulence, challenging established predictions and aligning with recent DNS results that reveal early lift reversal

https://doi.org/10.1017/jfm.2026.11410 Published online by Cambridge University Press

in deformable bubbles at lower Reynolds numbers (Tomiyama 1998; Du Cluzeau *et al.* 2019; Hidman *et al.* 2022).

Studies by Adoua, Legendre & Magnaudet (2009), Shi (2024) show that the direction of bubble migration is governed by the balance between the shear-induced lift force (F_L) and the pressure-gradient (or 'potential') force (F_P). The pressure-gradient force arises from the curvature of the mean carrier-flow velocity profile and always acts toward the centreline in duct and pipe flows. This is consistent with the transverse force decomposition in Shi & Magnaudet (2020) and Shi (2024), where the potential component never reverses sign. The lift force, in contrast, may change sign depending on the lift coefficient C_L. In a developing turbulent duct, we use the turbulence–Weber-based lift coefficient proposed by Salibindla *et al.* (2020), which is suitable for millimetric bubbles with moderate deformability. The corresponding lift force is

$$F_L(r) = \rho_\ell \, C_L(We) \, |\Delta w(r)| \, |\gamma(r)| \, V_b, \tag{4.17}$$

where $\Delta w(r)$ is the local slip velocity, $\gamma(r) = |\partial u_z/\partial r|$ is the local shear rate and V_b is the bubble volume. The sign of F_L is therefore controlled by the sign of C_L, which we evaluate using the correlation of Salibindla *et al.* (2020):

$$C_L = \begin{cases} 2.671\, We^{3/5}, & We < 0.1, \\ 1.25 - 1.608\, We^{3/5}, & 0.1 \le We < 0.9, \\ -0.23, & We \ge 0.9. \end{cases} \tag{4.18}$$

Here We is evaluated from (1.1). In all experimental cases and at all axial locations, a substantial fraction of bubbles falls in the regime We > 0.6, for which the lift coefficient becomes non-positive ($C_L \lesssim 0$), implying reversal of the lateral lift force.

Classically, core peaking is not expected for such small bubbles. For instance, Lu & Tryggvason (2006) found that nearly spherical bubbles remain wall peaked downstream in highly turbulent flows, and that a lift reversal – leading to core accumulation – requires $Eo \gg 1$ (i.e. significantly deformable bubbles of the order of 5–6 mm). Here, $Eo = (\rho_\ell - \rho_g)\, g\, d^2/\gamma$ is the Eötvös number, where g is gravity and ρ_g is air density, representing the ratio of buoyancy to surface-tension forces. However, their study does not address cases where $Eo \ll 1$, particularly in highly decaying flows, where turbulent dispersion has weakened to the extent that even a modest positive C_L drives bubble accumulation toward the core. As in this case, turbulence decays by over 90 % along the duct (see the monotonic drop in k/V^2 – see figure 6), and turbulent dispersion is dramatically weakened, allowing lift and wall forces to dominate and drive bubbles toward the core (Lu & Tryggvason 2006; Burns *et al.* 2004*a*).

The observed transition from uniform to core-peaked void fraction profiles arises from three key mechanisms: (i) as $\mathcal{I}$ diminishes (by $\sim$ 90 %), turbulent dispersion is weakened, losing its ability to homogenise the bubble distribution and allowing other forces to dominate; (ii) even micron-scale bubbles experience sufficient inward lift under low turbulence, overturning the conventional view that a critical bubble size ($\sim$5–6 mm) is necessary for lift reversal and core peaking, as recently confirmed by DNS (Du Cluzeau *et al.* 2019; Hidman *et al.* 2022); and (iii) as lift reversal takes hold, bubbles migrate toward the duct centreline, where upward liquid velocity is highest and drag is minimised, energetically favouring central accumulation (Lu & Tryggvason 2006). This drag-reduction mechanism is further reinforced by wall lubrication, which prevents bubble accumulation near the wall and maintains a depleted boundary region.

These findings not only depart from established wall-peaked paradigms seen in prior studies, but also suggest that the interplay of lift, wall-lubrication and turbulent-dispersion

https://doi.org/10.1017/jfm.2026.11410 Published online by Cambridge University Press

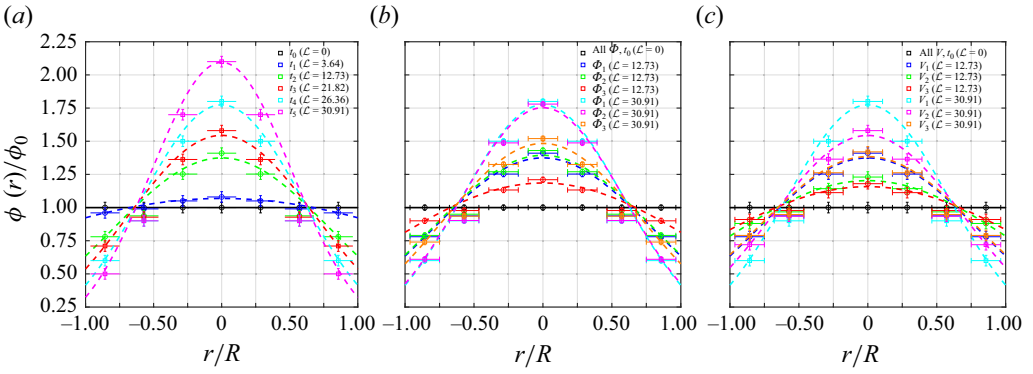


Figure 16. Transient radial variation of void fraction ($\phi(r)$) in a decaying turbulent regime. Parameters: sampling instants t_i are defined by $t_i = \mathcal{L}_i / V_1$ ($i = 0, \ldots, 5$). Bulk velocities: $V_1 = 6.1$, $V_2 = 7.4$, $V_3 = 8.4$ m s^{-1}. Axial locations: $\mathcal{L}_0 = 0$, $\mathcal{L}_1 = 3.64$, $\mathcal{L}_2 = 12.73$, $\mathcal{L}_3 = 21.82$, $\mathcal{L}_4 = 26.36$, $\mathcal{L}_5 = 30.91$. Results are shown for (*a*) $\phi(r)/\phi_0$ with $\mathcal{L}$ at $\phi = 0.5\,\%$ and $V = 6.1$ m s^{-1}, (*b*) $\phi(r)/\phi_0$ with ϕ at $V = 6.1$ m s^{-1}, (*c*) $\phi(r)/\phi_0$ with V at $\phi = 0.5\,\%$ & $\mathcal{L}$.

forces govern radial void fraction profiles even under extreme conditions. The present results thus fill an important gap in the literature, demonstrating persistent and robust core peaking even for micron-scale bubbles, a regime not previously reported, and provide new insight into dispersed phase redistribution mechanisms in turbulent multiphase flows.

In particular, the monotonic decrease of ϕ near the wall and its growth near the centre with increasing $\mathcal{L}$ raise important questions about the mechanisms driving migration from the wall toward the centre. This behaviour warrants further investigation by examining how radial distributions evolve under varying flow conditions and system parameters.

As bubbles migrate radially from the wall region (red) toward the duct centre (blue) (see figure 2*b*), the available cross-sectional area decreases. This geometric constraint leads to an amplification of local ϕ near the centre. Consequently, the radial variation of the local void fraction is inherently nonlinear. To quantitatively characterise this evolution, the measured radial void fraction profiles at each axial location ($\mathcal{L}$), void fraction (ϕ) and bulk velocity (V) were fitted to a Gaussian function (shown in figure 16):

$$\frac{\phi(r)}{\phi_o} = \Phi_i \exp\left(-\frac{(r/R - R_o)^2}{2\sigma^2}\right). \tag{4.19}$$

Here ϕ_0 is the cross-sectional mean, Φ_i is the peak amplitude (centreline void fraction), R_o is the mean position (fixed at zero by symmetry) and σ is the standard deviation describing the distribution width. The fitted parameters of figure 16 for all test cases are given in table 3. Figure 16 shows that near the duct inlet ($\mathcal{L} = 0$), the void fraction profile is nearly flat ($\Phi_i = 1, \sigma \to \infty$), confirming uniform bubble dispersion. Downstream, as $\mathcal{L}$ increases, Φ_i rises and σ decreases monotonically – indicating enhanced centreline peaking and profile narrowing due to turbulence decay, increased migration time and flow development. These trends are most pronounced at lower ϕ and V, as shown in figure 16(*a*).

It is interesting to note the effects of ϕ and V (figure 16*b*,*c*). For moderate ϕ ($\leq 1\,\%$), Φ_i and σ remain nearly unchanged with increasing ϕ, indicating self-similar profile shapes. However, at $\phi = 2\,\%$, the distribution broadens (σ increases) and the centreline amplitude decreases (Φ_i drops). This broadening arises from increased bubble–bubble interactions and, crucially, from stronger turbulent dispersion, which depends directly on the radial

https://doi.org/10.1017/jfm.2026.11410 Published online by Cambridge University Press

$\mathcal{L}$	ϕ	Φ_i	σ	$\mathcal{L}$	ϕ	Φ_i	σ	$\mathcal{L}$	V_i(m s^{-1})	Φ_i	σ
0	0.5 %	1.00	∞	0	All ϕ	1.00	∞	0	All V	1.0	∞
2.6	0.5 %	1.07	1.85	12.7	0.5 %	1.37	0.80	12.7	6.1	1.37	0.80
12.7	0.5 %	1.37	0.80	12.7	1 %	1.39	0.80	12.7	7.4	1.20	1.08
21.8	0.5 %	1.54	0.69	12.7	2 %	1.18	1.15	12.7	8.4	1.16	1.23
26.4	0.5 %	1.77	0.59	30.9	0.5 %	1.77	0.59	30.9	6.1	1.77	0.59
30.9	0.5 %	2.09	0.51	30.9	1 %	1.75	0.59	30.9	7.4	1.54	0.69
–	–	–	–	30.9	2 %	1.48	0.73	30.9	8.4	1.38	0.81
(*a*) $\phi(r)$ with $\mathcal{L}$ at $\phi = 0.5$ % & $V = 6.1$ m s^{-1}				(*b*) $\phi(r)$ with $\phi = 0.5$ %–2 % at $V = 6.1$ m s^{-1}				(*c*) $\phi(r)$ with V at $\phi = 0.5$ % & $\mathcal{L}$			

Table 3. Fitted parameters (refer to figure 16) of the normalised radial void fraction profiles for three different cases.

gradient $\Delta\phi(r)$. The dispersion flux is proportional to $-\nabla\phi_g$; so larger $\Delta\phi(r)$ (i.e. greater radial contrast) enhances outward mixing and inhibits further accumulation at the centre (Hosokawa & Tomiyama 2009). This self-regulating mechanism, where increased peaking amplifies dispersion, prevents unlimited core enrichment and is rarely captured in classical drift-flux models (Burns *et al.* 2004*a*; Ooms, Kewen & Mudde 2007; Hosokawa & Tomiyama 2009). A few recent DNS studies further confirm that bubble-driven dispersion follows Kolmogorov-like scaling and is modulated by radial gradients in the void fraction (Balachandar & Eaton 2010; Elghobashi 2019). Similarly, increasing V at fixed ϕ leads to lower Φ_i and higher σ, consistent with higher dissipation, stronger turbulent mixing and reduced migration time. Thus, broader, less-peaked distributions at high ϕ or V reflect the dominance of dispersion and bubble interactions over migration (Tomiyama *et al.* 2002; Du Cluzeau *et al.* 2019; Hidman *et al.* 2022).

The Gaussian parameterisation offers more than a compact description: it provides a direct link between observable profile shape and the balance between migration and dispersion mechanisms. The fitted σ quantifies the effectiveness of turbulent dispersion for given flow conditions, while Φ_i encodes the extent of core accumulation. These parameters are directly relevant for the calibration and validation of turbulence-dispersed two-phase flow models, including gradient-based closures (Burns *et al.* 2004*a*), and enable systematic comparison across modelling approaches. By relating σ to $\mathcal{I}$ and $\Delta\phi(r)$, this approach enables predictive scaling and cross-regime analysis, bridging detailed experiments, numerical simulations and practical engineering models.

5. Conclusions and future work

We studied an extreme, previously unexplored regime of developing bubbly flow: a high Re ($\approx 1.3 \times 10^5$) duct where pump-driven turbulence is initially intense ($I \geq 30$ %) and decays by $\sim$90 % downstream. This rapid decay shifts the interfacial dynamics from early fragmentation to sustained coalescence, driving a systematic evolution of the bubble size statistics and the void fraction field. The measurements provide a spatially resolved benchmark of how turbulence decays, and how coalescence kinetics and lateral migration jointly shape the bubble population.

In this highly turbulent, developing bubbly flow, the turbulent dissipation decreases with axial distance as $\varepsilon \sim \mathcal{L}^{-2}$, which is slightly slower than, but close to, the canonical HIT scaling ($\sim \mathcal{L}^{-2.2}$). Near the duct inlet, the bubble size PDF exhibits a mixed tail

https://doi.org/10.1017/jfm.2026.11410 Published online by Cambridge University Press

Symbol	Description
Flow parameters, velocity and turbulence	
u, v, w	Velocity components in x, y, z directions
$\overline{\mathbf{u}}$	Mean velocity vector
u', v', w'	Velocity fluctuation components in x, y, z directions
$\mathcal{U}$	Root mean square value of velocity fluctuations
$\mathcal{I}$, k and ε	Turbulence intensity, kinetic energy and dissipation
η, λ_T and ℓ	Kolmogorov length scale, Taylor microscale and integral length scale
Q_{air} and Q	Air volumetric flow rate and overall volumetric flow rate
$V = V_1, V_2, V_3$	Bulk velocity at 72 L min^{-1} (litres per minute), 87 L min^{-1} and 98 L min^{-1}
$\bar{V} = V_1 + V_2 + V_3/3$	Average velocity
$\mathcal{V} = V/\bar{V}$	Normalised velocity
$\phi = \phi_1, \phi_2, \phi_3$	Void fraction of 0.5 %, 1 % and 2 %
Physical properties	
ν and γ	Kinematic viscosity and surface tension
ρ_l, ρ_g	Liquid and gas density
Geometry and set-up	
y	Distance from the wall (wall-normal coordinate)
x and D	Axial position in duct and duct hydraulic diameter
$\mathcal{L} = x/D$	Normalised axial position
$t = \mathcal{L}/\mathcal{V}$	Residence time in the duct
b, l, δ	Channel width, axial and lateral positions
R_o	Mean position of Gaussian distribution
Bubble statistics	
d_{32} and $d_{99.8}$	Sauter mean diameter and 99.8th percentile bubble diameter
$d_{\max}$ and d_H	Maximum bubble diameter and Hinze scale
A	Projected 2D bubble area
n_i, N	Number of bubbles of diameter
$f(d)$	Modified Gaussian distribution function
Φ	Cumulative bubble size distribution
d_g and σ_g	Geometric mean and standard deviation of bubble diameters
Dimensionless and empirical quantities	
Re and Re_{λ}	Reynolds numbers (bulk, friction, and Taylor-scale)
We and We_{crit}	Weber number and critical Weber number
Γ, h	Coalescence rate and collision frequency
τ, T	Time period; averaging period

Table 4. List of symbols and their descriptions used in the paper.

with a $d^{-3/2}$ scaling in the sub-Hinze regime and a steeper $\sim d^{-10/3}$ scaling for super-Hinze bubbles; farther downstream, once the bubble population falls entirely below the Hinze scale, the PDF collapses to a single $d^{-3/2}$ scaling. Correspondingly, vigorous turbulence near the inlet promotes fragmentation, whereas as ε decays the flow evolves into a pure-coalescence region. In this transition, the bubble distribution initially straddles the Hinze scale, with turbulence-induced breakup limiting the largest sizes; downstream, as ε decreases, both d_{32} and $d_{99.8}$ grow sublinearly while remaining below d_{H}, confirming a coalescence-dominated regime. Theory and measurements jointly show that d_{32} and $d_{99.8}$ grow as $\sim\mathcal{L}^{0.5}$ in the present decaying turbulent flow, whereas the Hinze scale grows faster, $d_{\mathrm{H}} \sim \mathcal{L}^{0.9}$; because bubble sizes lag the rising breakup limit, breakup progressively weakens and the evolution trends toward pure coalescence. Consistent with this, the extreme-to-mean ratio $\mathcal{D}$ increases from $\sim$1.9 near the inlet (close to the pure-breakup regime, $\sim$1.8) to a universal plateau of $\approx$2.2 downstream (characteristic of pure coalescence), indicating the emergence of a quasi-self-similar spectrum. The cumulative

https://doi.org/10.1017/jfm.2026.11410 Published online by Cambridge University Press

distribution $\Phi(d/d_{32})$ exhibits a large log–log slope of $\sim$3.63 near the inlet together with a narrow width, reflecting a breakup-dominated behaviour. As the distribution relaxes, a characteristic slope of $\approx$1.3 appears only after $\mathcal{D}$ saturates and the spectrum stabilises, with this onset occurring earlier at larger ϕ. Over the same distance, the distribution width (σ_g) increases from about 1.48 near the inlet to about 2, again signalling a shift from breakup to coalescence. Although the Hinze limit increases rapidly with decaying ε ($d_{\mathrm{H}} \propto \varepsilon^{-2/5}$), the observed upper bubble size grows more slowly and always remains below the Hinze scale ($d_{99.8} < d_{\mathrm{H}}$), implying that breakup never completely disappears, since rare bubbles that exceed d_{H} are quickly fragmented. Meanwhile, the radial void fraction reorganises strongly: an initially near-uniform profile evolves into a sharply core-peaked, Gaussian-like distribution that narrows with $\mathcal{L}$, with increasing centreline ϕ and depletion near the wall. This persistent centre peaking, even for relatively small d_{32}, is consistent with early lift-force reversal in intense turbulence, aided by wall-lubrication effects that maintain near-wall depletion. Finally, increasing ϕ accelerates coalescence and shortens the relaxation length toward the universal spectrum, while a higher Reynolds number (bulk velocity V) sustains breakup for longer and tends to flatten radial segregation, although the net trend ultimately remains inward focusing as turbulence decays.

Overall, these results establish the coalescence-dominated, high-*Re* developing regime as a distinct operating window where a universal, sub-Hinze $d^{-3/2}$ spectrum and a core-peaked void profile emerge concomitantly with turbulence decay, filling a key gap in multiphase flow understanding and scale-up.

Acknowledgements. The authors thank Jacob Stancil and Jason Rom for their assistance with the experiments. This research used supporting resources at the Argonne Leadership Computing Facility and the Oak Ridge Leadership Computing Facility. The authors acknowledge the use of AI-based tools (e.g. Writefull, Grammarly, ChatGPT) strictly limited to spelling, grammar correction and paraphrasing; all technical content, analyses and conclusions are the authors' own.

Funding. The information, data or work presented herein was funded in part by the Advanced Research Projects Agency–Energy (ARPA-E), U.S. Department of Energy, under Award Number DE-AR0001587. The views and opinions of authors expressed herein do not necessarily state or reflect those of the United States Government or any agency thereof.

S. S. J acknowledges support from the donors of the ACS Petroleum Research Fund through Doctoral New Investigator Grant 69196-DNI9. The authors also acknowledge computing resources provided through the U.S. Department of Energy 2024 and 2025 ALCC awards (TUR147 and BubbleLaden). The Argonne Leadership Computing Facility at Argonne National Laboratory is supported by the Office of Science of the U.S. Department of Energy under Contract No. DE-AC02-06CH11357. The Oak Ridge Leadership Computing Facility at Oak Ridge National Laboratory is supported by the Office of Science of the U.S. Department of Energy under Contract No. DE-AC05-00OR22725.

Author contributions. **Vivek Kumar**: Conceptualisation, Methodology, Investigation, Experimental Setup Design, Data Curation, Formal Analysis, Visualisation, Writing—Original Draft & Review & Editing. **Prasoon Suchandra**: Data Curation and Analysis, Methodology, Writing—Review & Editing. **Ardalan Javadi**: Conceptualisation, Visualisation, Writing—Review & Editing. **Suhas S. Jain**: Supervision, Writing—Review & Editing. **Cyrus Aidun**: Conceptualisation, Supervision, Funding Acquisition, Project Administration, Writing—Review & Editing.

Declaration of interests. The authors report no conflict of interest.

Data availability. Data will be made available upon reasonable request to the corresponding author.

https://doi.org/10.1017/jfm.2026.11410 Published online by Cambridge University Press

Appendix A. Turbulent kinetic energy (k, near wall)

Figure 17 presents the axial variation of the normalised turbulent kinetic energy (k/V^2) near the duct wall.

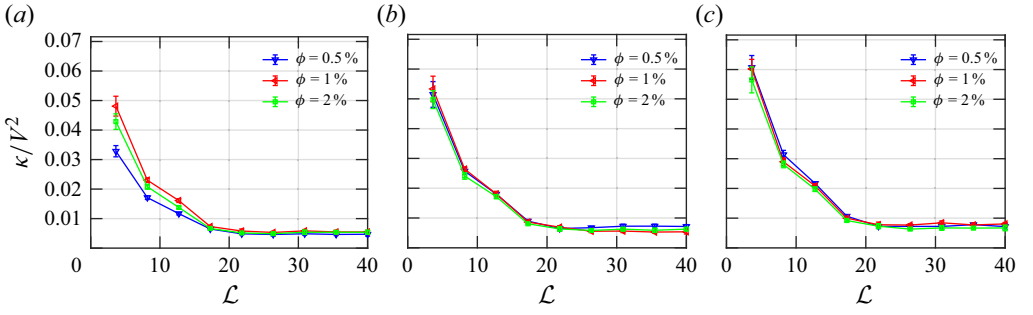


Figure 17. Axial variation of k near-wall plane for three bulk velocities $V(Q)$ and three void fractions ϕ. Results are shown for (*a*) $V = 6.1$ m s^{-1}, (*b*) $V = 7.4$ m s^{-1}, (*c*) $V = 8.4$ m s^{-1}.

Appendix B. Turbulent dissipation (ε, near wall)

Figure 18 presents the axial variation of the normalised turbulent dissipation rate ($(\varepsilon D)/\overline{V}^3$) near the duct wall.

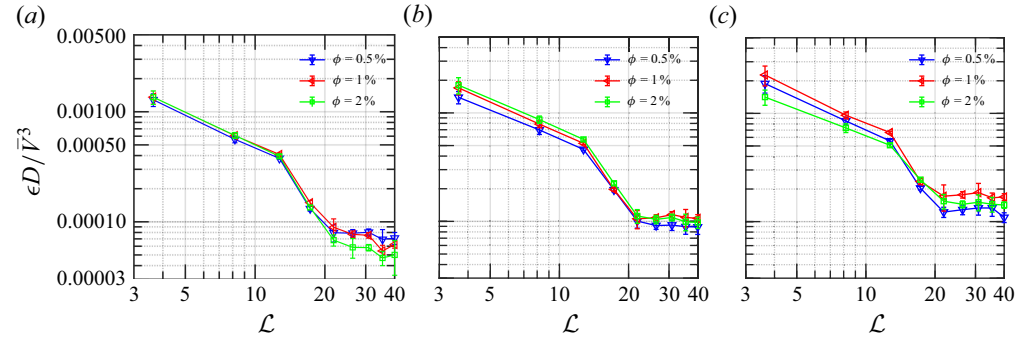


Figure 18. Axial variation of ε near-wall plane for three bulk velocities $V(Q)$ and three void fractions ϕ. Results are shown for (*a*) $V = 6.1$ m s^{-1}, (*b*) $V = 7.4$ m s^{-1}, (*c*) $V = 8.4$ m s^{-1}.

Appendix C. Bubble size growth in coalescence regime

C.1. *Turbulent collision kernel*

Effective rate of coalescence (= collision frequency (h) × coalescence efficiency (λ)) can be written as

$$\Gamma = h\,\lambda. \tag{C1}$$

The classical scaling (Kolmogorov 1991), originating with Kolmogorov and presented in standard treatments (Batchelor 1953; Monin & Yaglom 2013), underpins inertial-range collision models for bubbly dispersions. In the inertial subrange of turbulence, the velocity increment across a bubble scale d follows Kolmogorov's similarity hypothesis, which

https://doi.org/10.1017/jfm.2026.11410 Published online by Cambridge University Press

results in (Batchelor 1953; Monin & Yaglom 2013)

$$u_{rel}(d) \sim (\varepsilon\, d)^{1/3}, \tag{C2}$$

where ε is the mean dissipation rate. Multiplying the inertial-range relative speed by the geometric cross-section $\sim d^2$ gives the turbulent collision kernel

$$\beta \propto u_{rel}(d) \times d^2 \propto \varepsilon^{1/3}\, d^{7/3}, \tag{C3}$$

a form widely used in population-balance closures for bubble–bubble encounters in turbulent flows (Saffman & Turner 1956; Prince & Blanch 1990; Luo & Svendsen 1996). Furthermore, Prince & Blanch (1990) and Luo & Svendsen (1996) modelled the collision frequency for two bubbles of diameters d_i and d_j in isotropic turbulence as

$$h = C\,(\varepsilon)^{1/3}\,(d_i + d_j)^2 \cdot \sqrt{d_i^{\frac{2}{3}} + d_j^{\frac{2}{3}}}, \tag{C4}$$

where C is a constant. For a simplified scaling law, assuming a monodisperse system ($d_i = d_j = d$) results in $(d_i + d_j)^3 = (2d)^3 = 8d^3$, and Γ simplifies to

$$\Gamma = 8C\,\lambda\,(\varepsilon)^{1/3}\, d^{\frac{7}{3}}, \tag{C5}$$

with units of volume per time and $\lambda \in [0, 1]$. The spherical bubbles assumption is valid as the comparison of turbulent and interfacial time scales shows that the integral-scale eddy turnover time, $\tau_\ell = \ell/u'$, is $\mathcal{O}(10^{-2}\, s)$, while the bubble interfacial relaxation times, namely the capillary-inertial time scale $\tau_\gamma = (\rho d_{32}^3/\gamma)^{1/2}$ and the viscous-capillary time scale $\tau_\mu = \mu d_{32}/\gamma$, are $\mathcal{O}(10^{-3}\, s)$ (Kumar *et al.* 2026). Consequently, following coalescence, the bubble deformed interface relaxes quicker than the turbulent time scale, allowing it to reshape before a subsequent collision occurs.

C.2. *Population balance → diameter growth*

The number density n can be written using Smoluchowski's equation for binary coagulation (avoiding double counting and assuming monodisperse conditions) (Kreer & Penrose 1994):

$$\frac{\mathrm{d}n}{\mathrm{d}t} = -\frac{1}{2}\,\Gamma\, n^2. \tag{C6}$$

For a duct flow with mean velocity V, use $t = \mathcal{L}/\mathcal{V}$. Air-volume conservation relates n and d:

$$\phi = n\,\frac{\pi d^3}{6} \qquad \Rightarrow \qquad n = \frac{6\phi}{\pi d^3}. \tag{C7}$$

Eliminating n yields the identity (valid for any kernel):

$$\frac{\mathrm{d}n}{\mathrm{d}t} = \frac{\mathrm{d}n}{\mathrm{d}d}\,\frac{\mathrm{d}d}{\mathrm{d}t} = \frac{\mathrm{d}}{\mathrm{d}d}\left(\frac{6\phi}{\pi d^3}\right)\frac{\mathrm{d}d}{\mathrm{d}t} = -\frac{18\phi}{\pi d^4}\,\frac{\mathrm{d}d}{\mathrm{d}t}. \tag{C8}$$

After simplification,

$$\frac{\mathrm{d}d}{\mathrm{d}\mathcal{L}} = \frac{\Gamma\phi}{\mathcal{V}\pi\, d^2}. \tag{C9}$$

Inserting $\Gamma = 8C\,\lambda(\varepsilon)^{1/3} d^{\frac{7}{3}}$ gives

$$\frac{\mathrm{d}d}{\mathrm{d}\mathcal{L}} = \frac{8C}{\pi\mathcal{V}}\,\lambda\,\phi\,(\varepsilon)^{1/3}\, d^{\frac{1}{3}}. \tag{C10}$$

https://doi.org/10.1017/jfm.2026.11410 Published online by Cambridge University Press

The bubble diameter growth law with decaying turbulence ($\varepsilon \to \varepsilon(\mathcal{L})$):

$$\frac{\mathrm{d}d}{\mathrm{d}\mathcal{L}} = K_o[\varepsilon(\mathcal{L})]^{1/3} d^{\frac{1}{3}}, \quad \text{where} \quad K_o = \frac{8C}{\pi \mathcal{V}} \lambda \phi. \tag{C11}$$

C.3. *Simplifying coalescence efficiency (λ)*

The coalescence efficiency can be described by the widely known film drainage model,

$$\lambda_{ij} = \exp\left(-\frac{t_{drain}}{t_{contact}}\right), \tag{C12}$$

where t_{drain} is the time for the intervening liquid film to thin to rupture thickness and $t_{contact}$ is the hydrodynamic contact time during a collision (Lehr *et al.* 2002). In bubbly turbulence with deformable, mobile interfaces, film drainage formulations distinguish regimes by interfacial mobility; for gas bubbles in clean liquids, the relevant asymptote is the inertia-controlled drainage limit (Chesters 1991; Liao & Lucas 2010; Chan, Klaseboer & Manica 2011).

C.3.1. *Drainage time (deformable, inertia–controlled)*

Using Chesters (1991) parallel-film model in the inertia limit, the drainage time reduces to

$$t_{drain} = \frac{1}{2} \frac{\rho_c \, u_{rel} \, r^2}{\gamma}, \qquad r = \frac{d}{2}, \tag{C13}$$

with continuous-phase density ρ_c, surface tension γ, bubble radius r and approach speed u_{rel} (Liao & Lucas 2010). (For unequal sizes, see the (Luo 1995) generalisation; here we restrict to monodisperse.)

C.3.2. *Contact time and approach velocity*

A standard turbulent contact time is

$$t_{contact} \sim \frac{d^{2/3}}{\varepsilon^{1/3}}, \tag{C14}$$

and an inertial-range estimate for the approach velocity is

$$u_{rel} \approx \sqrt{2} \left[\varepsilon \, (2d)\right]^{1/3}. \tag{C15}$$

With monodisperse simplification ($d_i = d_j = d$), and combining (C13)–(C15), gives

$$\frac{t_{drain}}{t_{contact}} = \frac{\rho_c}{\sigma} \, 2^{-13/6} \, \varepsilon^{2/3} \, d^{5/3}, \tag{C16}$$

$$\Rightarrow \quad \lambda(d) = \exp\Big[- A \, \frac{\rho_c}{\sigma} \, \varepsilon^{2/3} \, d^{5/3} \Big], \qquad A = 2^{-13/6} \approx 0.223. \tag{C17}$$

C.3.3. *Numerical constants for water (20°C)*

Using $\rho_c = 998 \, \mathrm{kg} \, m^{-3}$ and $\gamma = 0.072 \, \mathrm{N} \, m^{-1}$ (air–water), (C17) is fully specified.

C.3.4. *Examples (equal sizes)*

(i) Case A (72 L min^{-1} and 0.5 %) at $\mathcal{L} = 0$**:** $\varepsilon = 200 \, \mathrm{m}^2 \, s^{-3}$, $d = 200 \, \mu$m. From (C15) $u_{rel} \approx 0.609 \, \mathrm{m} \, s^{-1}$; using (C13) and (C14), $t_{drain} \approx 4.22 \times 10^{-5}$ s, $t_{contact} \approx 5.85 \times$

https://doi.org/10.1017/jfm.2026.11410 Published online by Cambridge University Press

ε scaling	$d(d_{32}$ and $d_{99.8})$ scaling
$\varepsilon \propto \mathcal{L}^{-m}$	$d \propto \mathcal{L}^{\beta}$, $\beta = 3 - m/2$
$\varepsilon \propto \mathcal{L}^{-1.8}$	$d \propto \mathcal{L}^{3/5}$
$\varepsilon \propto \mathcal{L}^{-2}$	$d \propto \mathcal{L}^{1/2}$
$\varepsilon \propto \mathcal{L}^{-2.2}$	$d \propto \mathcal{L}^{2/5}$

Table 5. Bubble diameter scaling in highly decaying turbulent flow.

10^{-4} s, so

$$\lambda = \exp\left(-\frac{t_{drain}}{t_{contact}}\right) \approx \exp(-0.072) \approx \mathbf{0.93}. \tag{C18}$$

(ii) Case B (72 L min^{-1} and 0.5 %) at $\mathcal{L} = 40$**:** $\varepsilon = 10\,\mathrm{m}^2\,\mathrm{s}^{-3}$, $d = 500\,\mu$m. $u_{rel} \approx$ 0.305 m s^{-1}, $t_{drain} \approx 1.32 \times 10^{-4}$ s, $t_{contact} \approx 2.92 \times 10^{-3}$ s, hence,

$$\lambda \approx \exp(-0.045) \approx \mathbf{0.95}. \tag{C19}$$

Hence, it can be concluded that λ remains high and constant for our scaling regime. The high coalescence efficiency results from the film drainage time, t_{drain}, being significantly shorter than the contact time, $t_{contact}$, associated with the eddy turnover time.

Hence, we have,

$$\lambda \sim \text{constant}, \quad \Rightarrow \quad K_o \sim \text{constant (2)} \tag{C20}$$

C.4. *Solving the population-balance equation*

Using the decay as a power law referenced to a finite start time $\mathcal{L} > 0$ (see (4.5)), i.e.

$$\varepsilon(t) = \varepsilon_0 \left(\mathcal{L}\right)^{-m}, \qquad \varepsilon_0 \equiv \varepsilon(\mathcal{L}), \tag{C21}$$

then simplifying (C10),

$$\frac{1}{d^{1/3}} \frac{\mathrm{d}d}{\mathrm{d}\mathcal{L}} = K_o (\varepsilon_0)^{1/3} \mathcal{L}^{-m/3}, \tag{C22}$$

$$d(\mathcal{L}) = \left[d_0^{2/3} + K_o (\varepsilon_0)^{1/3} \int_{\mathcal{L}_0}^{\mathcal{L}} \mathcal{L}^{-m/3}\, d\mathcal{L} \right]^{3/2}, \tag{C23}$$

$$d(\mathcal{L}) = \left[d_0^{2/3} + K_o\, \varepsilon_0^{1/3} \mathcal{L}_0^{1/3} \left(\mathcal{L}^{\frac{3-m}{3}} - \mathcal{L}_0^{\frac{3-m}{3}} \right) \right]^{3/2}, \tag{C24}$$

$$d(\mathcal{L}) \propto \mathcal{L}^{\frac{3-m}{2}} \propto \mathcal{L}^{\beta}, \quad \text{here} \quad \beta = \frac{3-m}{2}. \tag{C25}$$

C.4.1. *Case A:* $\varepsilon \propto \mathcal{L}^{-1.8}$ *(*$m = 1.8$*)*

In this case, simplifying (C22) yields,

$$\int_{\mathcal{L}_0}^{\mathcal{L}} \mathcal{L}^{-0.6} \mathrm{d}\mathcal{L} = \frac{5}{2} \left(\mathcal{L}^{0.4} - \mathcal{L}_0^{0.4} \right), \tag{C26}$$

$$d(\mathcal{L}) = \left[d_0^{2/3} + K_o\, \varepsilon_0^{1/3} \mathcal{L}_0^{1/3} \left(\mathcal{L}^{0.4} - \mathcal{L}_0^{0.4} \right) \right]^{3/2}, \tag{C27}$$

$$d(\mathcal{L}) \propto \mathcal{L}^{0.6}. \tag{C28}$$

https://doi.org/10.1017/jfm.2026.11410 Published online by Cambridge University Press

C.4.2. *Case B:* $\varepsilon \propto \mathcal{L}^{-2}$ $(m = 2)$
In this case, simplifying (C22) yields,

$$\int_{\mathcal{L}_0}^{\mathcal{L}} \mathcal{L}^{-0.67} \mathrm{d}\mathcal{L} = \frac{10}{3}\left(\mathcal{L}^{0.33} - \mathcal{L}_0^{0.33}\right), \tag{C29}$$

$$d(\mathcal{L}) = \left[d_0^{2/3} + K_o\, \varepsilon_0^{1/3} \mathcal{L}_0^{1/3}\left(\mathcal{L}^{0.33} - \mathcal{L}_0^{0.33}\right)\right]^{3/2}, \tag{C30}$$

$$d(\mathcal{L}) \propto \mathcal{L}^{0.5}. \tag{C31}$$

C.4.3. *Case C:* $\varepsilon \propto \mathcal{L}^{-2.2}$ $(m = 2.2)$
In this case, simplifying (C22) yields,

$$\int_{\mathcal{L}_0}^{\mathcal{L}} \mathcal{L}^{-0.73} \mathrm{d}\mathcal{L} = \frac{10}{2.7}\left(\mathcal{L}^{0.27} - \mathcal{L}_0^{0.27}\right), \tag{C32}$$

$$d(\mathcal{L}) = \left[d_0^{2/3} + K_o\, \varepsilon_0^{1/3} \mathcal{L}_0^{1/3}\left(\mathcal{L}^{0.27} - \mathcal{L}_0^{0.27}\right)\right]^{3/2},$$

$$d(\mathcal{L}) \propto \mathcal{L}^{0.4}. \tag{C33}$$

References

Adoua, R., Legendre, D. & Magnaudet, J. 2009 Reversal of the lift force on an oblate bubble in a weakly viscous linear shear flow. *J. Fluid Mech.* **628**, 23–41.

Alameedy, U., Al-Sarkhi, A. & Abdul-Majeed, G. 2025 Comprehensive review of severe slugging phenomena and innovative mitigation techniques in oil and gas systems. *Chem. Engng Res. Des.* **213**, 78–94.

Alméras, E., Mathai, V., Lohse, D. & Sun, C. 2017 Experimental investigation of the turbulence induced by a bubble swarm rising within incident turbulence. *J. Fluid Mech.* **825**, 1091–1112.

Angulo, A., van der, L., Peter, G., Han, M.M. & D.F., Rivas 2020 Influence of bubbles on the energy conversion efficiency of electrochemical reactors. *Joule* **4** (3), 555–579.

Balachandar, S. & Eaton, J.K. 2010 Turbulent dispersed multiphase flow. *Annu. Rev. Fluid Mech.* **42** (1), 111–133.

Batchelor, G.K. 1953 *The Theory of Homogeneous Turbulence*. Cambridge University Press.

Batchelor, G.K. & Proudman, I. 1956 The large-scale structure of homogenous turbulence. *Phil. Trans. R. Soc. Lond. Series A Math. Phys. Sci.* **248** (949), 369–405.

Bouche, E., Roig, V., Risso, F. & Billet, A.-M. 2012 Homogeneous swarm of high-Reynolds-number bubbles rising within a thin gap. Part 1. Bubble dynamics. *J. Fluid Mech.* **704**, 211–231.

Bouche, E., Roig, V., Risso, F. & Billet, A.-M. 2014 Homogeneous swarm of high-Reynolds-number bubbles rising within a thin gap. Part 2. Liquid dynamics. *J. Fluid Mech.* **758**, 508–521.

Bröder, D. & Sommerfeld, M. 2004 Examination of bubble collisions and coalescence in bubbly flows. In *Bubbly Flows: Analysis, Modelling and Calculation*, pp. 21–36. Springer.

Brown, C.S. & Bolotnov, I.A. 2015 Spectral analysis of the turbulent energy spectrum in single and two-phase bubbly flows in different geometries based on direct numerical simulation results. In *16th International Topical Meeting on Nuclear Reactor Thermal Hydraulics (NURETH-16)*, pp. 7129–7142. American Nuclear Society.

Bunner, B. & Tryggvason, G. 2002 Dynamics of homogeneous bubbly flows Part 1. Rise velocity and microstructure of the bubbles. *J. Fluid Mech.* **466**, 17–52.

Bunner, B. & Tryggvason, G. 2003 Effect of bubble deformation on the properties of bubbly flows. *J. Fluid Mech.* **495**, 77–118.

Burns, A.D., Frank, T., Hamill, I. & Shi, J.M. 2004*a* Turbulent dispersion in bubbly two-phase flows. *Intl J. Multiphase Flow* **30** (6), 795–825.

Burns, A.D., Frank, T., Hamill, I., Shi, J.-M., 2004*b* The Favre averaged drag model for turbulent dispersion in Eulerian multi-phase flows. In *5th International Conference on Multiphase Flow*, vol. 4, pp. 1–17. ICMF.

Calado, A. & Balaras, E. 2024 Dynamics of bubble deformation and breakup in decaying isotropic turbulence. *Phys. Rev. Fluids* **9** (12), 123604.

https://doi.org/10.1017/jfm.2026.11410 Published online by Cambridge University Press

CHAN, D.Y.C., KLASEBOER, E. & MANICA, R. 2011 Film drainage and coalescence between deformable drops and bubbles. *Soft Matt.* **7** (6), 2235–2264.

CHAN, W.H.R., DODD, M.S., JOHNSON, P.L., URZAY, J. & MOIN, P. 2018 Formation and dynamics of bubbles in breaking waves: Part II. The evolution of the bubble size distribution and breakup/coalescence statistics. *Annu. Res. Briefs* **2018**, 21–34.

CHEN, H., WEI, S., DING, W., WEI, H., LI, L., SAXÉN, H., LONG, H. & YU, Y. 2021 Interfacial area transport equation for bubble coalescence and breakup: developments and comparisons. *Entropy* **23**, 1106.

CHEN, P.-C., JHUANG, J.-H., WU, T.-W., YANG, C.-Y., WANG, K.-Y. & CHEN, C.-M. 2023 Capture of CO2 using mixed amines and solvent regeneration in a lab-scale continuous bubble-column scrubber. *Appl. Sci.* **13** (12), 7321.

CHESTERS, A_K. 1991 Modelling of coalescence processes in fluid-liquid dispersions: a review of current understanding. *Chem. Engng Res. Des.* **69** (A4), 259–270.

CHIECO, A.T. & DURIAN, D.J. 2023 Simply solvable model capturing the approach to statistical self-similarity for the diffusive coarsening of bubbles, droplets, and grains. *Phys. Rev. E* **108** (3), 034606.

CLIFT, R., GRACE, J.R. & WEBER, M.E. 2005 *Bubbles, Drops, and Particles*. Dover Publications.

COULALOGLOU, C.A. & TAVLARIDES, L.L. 1977 Description of interaction processes in agitated liquid-liquid dispersions. *Chem. Engng Sci.* **32**, 1289–1297.

CRIALESI-ESPOSITO, M., CHIBBARO, S. & BRANDT, L. 2023 The interaction of droplet dynamics and turbulence cascade. *Commun. Phys.* **6** (1), 5.

DABIRI, S., LU, J. & TRYGGVASON, G. 2013 Transition between regimes of a vertical channel bubbly upflow due to bubble deformability. *Phys. Fluids* **25** (10), 102110.

DE TEMMERMAN, L., MAERE, T., TEMMINK, H., ZWIJNENBURG, A. & NOPENS, I. 2015 The effect of fine bubble aeration intensity on membrane bioreactor sludge characteristics and fouling. *Water Res.* **76**, 99–109.

DEANE, G.B. & STOKES, M.D. 2002 Scale dependence of bubble creation mechanisms in breaking waves. *Nature* **418**, 839–844.

DELNOIJ, E., KUIPERS, J.A.M., VAN SWAAIJ, W.P.M. & AKKER, H.E.A. 1997 Computational fluid dynamics applied to gas–liquid contactors. *Chem. Engng Sci.* **52** (21-22), 3623–3638.

DIAZ, O., GONZALEZ, E. & VERA, L. 2024 Influence of air scouring and residual fouling on cake build-up and compression in membrane bioreactors. *Ind. Engng Chem. Res.* **63** (31), 13740–13751.

DING, L., VAN BUREN, T., GUNADY, I.E. & SMITS, A.J. 2021 Perspective on the response of turbulent pipe flows to strong perturbations. *Fluids* **6** (6), 208.

DOHERTY, J., NGAN, P., MONTY, J. & CHONG, M. 2007 The development of turbulent pipe flow. In *16th Australasian Fluid Mechanics Conference*, pp. 266–270.

DU CLUZEAU, A., BOIS, G. & TOUTANT, A. 2019 Analysis and modelling of Reynolds stresses in turbulent bubbly up-flows from direct numerical simulations. *J. Fluid Mech.* **866**, 132–168.

DURST, F., JOVANOVIĆ, J. & SENDER, J. 1995 LDA measurements in the near-wall region of a turbulent pipe flow. *J. Fluid Mech.* **295**, 305–335.

EGGELS, J.G.M., UNGER, F., WEISS, M.H., WESTERWEEL, J., ADRIAN, R.J., FRIEDRICH, R. & NIEUWSTADT, F.T.M. 1994 Fully developed turbulent pipe flow: a comparison between direct numerical simulation and experiment. *J. Fluid Mech.* **268**, 175–210.

ELGHOBASHI, S. 2019 Direct numerical simulation of turbulent bubbly flows. *Annu. Rev. Fluid Mech.* **51**, 217–244.

ESTEVADEORDAL, J. & GOSS, L. 2005 PIV with LED: Particle shadow velocimetry (PSV). In *43rd AIAA Aerospace Sciences Meeting and Exhibit*.

EVANS, G.M., JAMESON, G.J. & ATKINSON, B.W. 1992 Prediction of the bubble size generated by a plunging liquid jet bubble column. *Chem. Engng Sci.* **47** (13-14), 3265–3272.

FABRE, J. & LINÉ, A. 1992 Modeling of two-phase slug flow. *Annu. Rev. Fluid Mech.* **24**, 21–46.

FARSOIYA, P.K., LIU, Z., DAISS, A., FOX, R.O. & DEIKE, L. 2023 Role of viscosity in turbulent drop break-up. *J. Fluid Mech.* **972**, A11.

FRIEDLANDER, S.K., 2000 *Smoke, Dust, and Haze*, vol. 198. Oxford University Press New York.

GARCIA-OCHOA, F. & GOMEZ, E. 2009 Bioreactor scale-up and oxygen transfer rate in microbial processes: an overview. *Biotechnol. Adv.* **27** (2), 153–176.

GARRETT, C. & LI, M. 2000 Connection between bubble size spectra and energy dissipation rates in the upper ocean. *J. Phys. Oceanogr.* **30** (9), 2163–2171.

GAVRILAKIS, S. 1992 Numerical simulation of low-Reynolds-number turbulent flow through a straight square duct. *J. Fluid Mech.* **244**, 101–129.

GEORGE, W.K. & HUSSEIN, H.J. 1991 Locally axisymmetric turbulence. *J. Fluid Mech.* **233**, 1–23.

https://doi.org/10.1017/jfm.2026.11410 Published online by Cambridge University Press

GUO, X., ZHOU, Q., LI, J. & CHEN, C. 2016 Implementation of an improved bubble breakup model for TFM-PBM simulations of gas–liquid flows in bubble columns. *Chem. Engng Sci.* **152**, 255–266.
HAGESAETHER, L., JAKOBSEN, H.A., HJARBO, K. & SVENDSEN, H.F. 2000 A coalescence and breakup module for implementation in CFD-codes. In *Computer Aided Chemical Engineering*, vol. 8, pp. 367–372. Elsevier.
HESKETH, R.P., ETCHELLS, A.W. & RUSSELL, T.B. 1987 Bubble breakage in pipeline flow. *Chem. Engng Sci.* **42** (3), 649–653.
HESSENKEMPER, H. & ZIEGENHEIN, T. 2018 Particle shadow velocimetry (PSV) in bubbly flows. *Intl J. Multiphase Flow* **106**, 268–279.
HIBIKI, T. & ISHII, M. 1999 Experimental study on interfacial area transport in bubbly two-phase flows. *Intl J. Heat Mass Transfer* **42** (16), 3019–3035.
HIDMAN, N., STRÖM, H., SASIC, S. & SARDINA, G. 2022 The lift force on deformable and freely moving bubbles in linear shear flows. *J. Fluid Mech.* **952**, A34.
HINZE, J.O. 1955 Fundamentals of the hydrodynamic mechanism of splitting in dispersion processes. *AIChE J.* **1** (3), 289–295.
HINZE, J.O. 1975 *Turbulence*, 2nd edn. McGraw-Hill.
HOSOKAWA, S. & TOMIYAMA, A. 2009 Multi-fluid simulation of turbulent bubbly pipe flows. *Chem. Engng Sci.* **64** (24), 5308–5318.
JAIN, S.S. & ELNAHHAS, A. 2025 Stationary states of forced two-phase turbulence. *Chem. Engng J.* **524**, 169077.
JASSAL, G.R., SONG, M. & SCHMIDT, B.E. 2025 Particle shadow velocimetry and its potential applications, limitations and advantages vis-à-vis particle image velocimetry. *Exp. Fluids* **66** (1), 21.
JAVADI, A., KUMAR, V. & AIDUN, C.K. 2026 Large eddy simulations of side channel pump in different operating conditions. *Engng Appl. Comput. Fluid* **20** (1), 2587723.
KAMP, A.M., CHESTERS, A.K. & COLIN, C. 2001 Bubble coalescence in turbulent flows: a mechanistic model for turbulence-induced coalescence applied to microgravity bubbly pipe flow. *Intl J. Multiphase Flow* **27** (8), 1363–1396.
KANTARCI, N., BORAK, F. & ULGEN, K.O. 2005 Bubble column reactors. *Process Biochem.* **40** (7), 2263–2283.
KHODAPARAST, S., BORHANI, N., TAGLIABUE, G. & THOME, J.R. 2013 A micro particle shadow velocimetry (μPSV) technique to measure flows in microchannels. *Exp. Fluids* **54**, 1474.
KIM, Y. & PARK, H. 2021 Deep learning-based automated and universal bubble detection and mask extraction in complex two-phase flows. *Sci. Rep.* **11** (1), 8940.
KLEINSTREUER, C. & AGARWAL, R.K. 2001 Modelling of the coalescence/redispersion processes in bubble columns. *Chem. Engng Sci.* **56** (3), 1085–1093.
KOLMOGOROV, A.N. 1941*a* Dissipation of energy in the locally isotropic turbulence. In *Proceedings of the USSR Academy of Sciences*, pp. 16–18, vol. 32.
KOLMOGOROV, A.N. 1941*b* The local structure of turbulence in incompressible viscous fluid for very large Reynolds numbers. *Proc. USSR Acad. Sci.* **30**, 299–303.
KOLMOGOROV, A.N. 1949 On the breakage of droplets in a turbulent flow. *Dokl. Akad. Nauk SSSR* **66**, 825–828.
KOLMOGOROV, A.N. 1962 A refinement of previous hypotheses concerning the local structure of turbulence in a viscous incompressible fluid at high Reynolds number. *J. Fluid Mech.* **13**, 82–85.
KOLMOGOROV, A.N. 1991 The local structure of turbulence in incompressible viscous fluid for very large Reynolds numbers. *Proc. R. Soc. Lond. Series A: Math. Phys. Sci.* **434** (1890), 9–13.
KREER, M. & PENROSE, O. 1994 Proof of dynamical scaling in Smoluchowski's coagulation equation with constant kernel. *J. Stat. Phys.* **75** (3), 389–407.
KULKARNI, A.A. 2007 Mass transfer in bubble column reactors: effect of bubble size distribution. *Ind. Engng Chem. Res.* **46** (7), 2205–2211.
KUMAR, V., JAIN, P., UPADHYAY, R.K., BHARATH, K.S. & WAGHMARE, P.R. 2023 Particle separation using modified Taylor's flow. *Microfluid. Nanofluid.* **27** (10), 66.
KUMAR, V., QUINTERO, J., BALDYGIN, A., MOLINA, P., WILLERS, T. & WAGHMARE, P.R. 2026 Viscosity and dynamic surface tension measurement: a guideline for appropriate measurement. *J. Colloid Interface Sci.* 139929.
LAAKKONEN, M., MOILANEN, P. & AITTAMAA, J. 2005 Local bubble size distributions in agitated vessels. *Chem. Engng J.* **106** (2), 133–143.
LAAKKONEN, M., ALOPAEUS, V. & AITTAMAA, J. 2006 Validation of bubble breakage, coalescence and mass transfer models for gas–liquid dispersion in agitated vessel. *Chem. Engng Sci.* **61** (1), 218–228.

https://doi.org/10.1017/jfm.2026.11410 Published online by Cambridge University Press

LAAKKONEN, M., ALOPAEUS, V. & AITTAMAA, J. 2007*a* Validation of bubble coalescence and breakup models in stirred gas–liquid dispersion. *Chem. Engng Sci.* **62**, 721–740.

LAAKKONEN, M., MOILANEN, P., ALOPAEUS, V. & AITTAMAA, J. 2007*b* Modelling local bubble size distributions in agitated vessels. *Chem. Engng Sci.* **62** (3), 721–740.

LANCE, M. & BATAILLE, J. 1991 Turbulence in the liquid phase of a uniform bubbly air–water flow. *J. Fluid Mech.* **222**, 95–118.

LAVOIE, P., AVALLONE, G., GREGORIO, F.DE, ROMANO, G.P. & ANTONIA, R.A. 2007 Spatial resolution of piv for the measurement of turbulence. *Exp. Fluids* **43**, 39–51.

LEE, T. 2020 Lognormality in turbulence energy spectra. *Entropy* **22** (6), 669.

LEHR, F., MILLIES, M. & MEWES, D. 2002 Bubble-size distributions and flow fields in bubble columns. *AIChE J.* **48** (11), 2426–2443.

LI, S. & LIAO, Y. 2024 CFD investigation of bubble breakup and coalescence in a rectangular pool-scrubbing column. *Nucl. Engng Des.* **425**, 113342.

LI, Y., LIU, Z., XU, G. & LI, B. 2024 Effect of breakup and coalescence kernels on polydispersed bubbly flow in continuous casting mold. *Intl J. Multiphase Flow* **177**, 104872.

LIAO, Y. & LUCAS, D. 2009 A literature review of theoretical models for drop and bubble breakup in turbulent dispersions. *Chem. Engng Sci.* **64**, 3389–3406.

LIAO, Y. & LUCAS, D. 2010 A literature review on mechanisms and models for the coalescence process of fluid particles. *Chem. Engng Sci.* **65** (10), 2851–2864.

LIBERZON, A., 2020 OpenPIV/openpiv-python: OpenPIV - Python (v0.22.2) with a new extended search PIV grid option (0.22.2). *Zenodo* **3930343**.

LOITSYANSKII, L.G. 1939 Some fundamental laws of isotropic turbulent flow. *Trans TZAGI* **440**, 3–23.

LU, J. & TRYGGVASON, G. 2006 Numerical study of turbulent bubbly downflows in a vertical channel. *Phys. Fluids* **18** (10), 103302.

LUCAS, D., BEYER, M. & SZALINSKI, L. 2023 Experiments on gas–liquid flow in vertical pipes. In *Handbook of Multiphase Flow Science and Technology*, pp. 625–669. Springer.

LUO, H. 1995 Coalescence, breakup and liquid circulation in bubble column reactors. PhD thesis, Norwegian University of Science and Technology (NTNU).

LUO, H. & SVENDSEN, H.F. 1996 Theoretical model for drop and bubble breakup in turbulent dispersions. *AIChE J.* **42** (5), 1225–1233.

MARTÍNEZ-BAZÁN, C., MONTA NÉS, J.L. & LASHERAS, J.C. 1999 Breakup of an air bubble injected into a fully developed turbulent flow. Part 1: breakup frequency. *J. Fluid Mech.* **401**, 157–182.

MATIAZZO, T., DECKER, R.K., BASTOS, J.C.S.C., SILVA, M.K. & MEIER, H. 2020 Investigation of breakup and coalescence models for churn-turbulent gas–liquid bubble columns. *J. Appl. Fluid Mech.* **13** (2), 737–751.

MONIN, A.S. & YAGLOM, A. 2013 *Statistical Fluid Mechanics, Volume II: Mechanics of Turbulence*, vol. 2. Courier Corporation.

NA, B., CHANG, K.-A. & LIM, H.-J. 2022 Comparison of flow dynamics and air entrainment under laboratory plunging and spilling breaking waves. *Coastal Engng Proc.* **37**, 13–13.

NAMBIAR, D.K.R., KUMAR, R. & GANDHI, K.S. 1990 Breakage and coalescence of drops in turbulent stirred dispersions. *Sadhana* **15**, 73–103.

NGUYEN, V.T., SONG, C.-H., BAE, B.-U. & EUH, D.-J. 2013 Modeling of bubble coalescence and break-up considering turbulent suppression phenomena in bubbly two-phase flow. *Intl J. Multiphase Flow* **54**, 31–42.

NI, R. 2024 Deformation and breakup of bubbles and drops in turbulence. *Annu. Rev. Fluid Mech.* **56** (1), 319–347.

OBUKHOV, A.M. 1941 On the spectral energy distribution in a turbulent flow. *Izv. Akad. Nauk SSSR, Geogr. Geofiz.* **5**, 453–466.

OBUKHOV, A.M. 1962 Some specific features of atmospheric turbulence. *J. Geophys. Res.* **67** (8), 3011–3014.

OOMS, G., KEWEN, S. & MUDDE, R.F. 2007 The effect of turbulent dispersion on phase distribution in vertical two-phase pipe flow. *Intl J. Multiphase Flow* **33** (5), 473–489.

OWOLABI, B.E., POOLE, R.J. & DENNIS, D.J.C. 2016 Experiments on low-Reynolds-number turbulent flow through a square duct. *J. Fluid Mech.* **798**, 398–410.

POPE, S.B. 2000 *Turbulent Flows*. Cambridge University Press.

PRAKASH, V.N., MARTINEZ MERCADO, J., VAN WIJNGAARDEN, L., MANCILLA, E., TAGAWA, Y., LOHSE, D. & SUN, C. 2016 Energy spectra in turbulent bubbly flows. *J. Fluid Mech.* **791**, 174–190.

PRINCE, M.J. & BLANCH, H.W. 1990 Bubble coalescence and break-up in air-sparged bubble columns. *AIChE J.* **36** (10), 1485–1499.

RAZZAQUE, A., BRÖDER, D. & SOMMERFELD, M. 2003*a* Experimental investigations on bubble coalescence and break-up in turbulent dispersion. *Intl J. Multiphase Flow* **29**, 305–321.

https://doi.org/10.1017/jfm.2026.11410 Published online by Cambridge University Press

RAZZAQUE, M.M., TOMIYAMA, A. & KATAOKA, I. 2003*b* Bubble size in coalescence dominant regime of turbulent air–water flow through horizontal pipes. *Intl J. Multiphase Flow* **29** (9), 1451–1471.
RISSO, F. 2018 Agitation, mixing, and transfers induced by bubbles. *Annu. Rev. Fluid Mech.* **50**, 25–48.
RISSO, F. & FABRE, J. 1998 Oscillations and breakup of a bubble immersed in a turbulent field. *J. Fluid Mech.* **372**, 323–355.
ROCCON, A., ZONTA, F. & SOLDATI, A. 2023 Phase-field modeling of complex interface dynamics in drop-laden turbulence. *Phys. Rev. Fluids* **8** (9), 090501.
RONG, W., LI, Z., ZHANG, W. & SUN, L. 2014 An improved canny edge detection algorithm. In *2014 IEEE International Conference on Mechatronics and Automation*, pp. 577–582. IEEE.
RUIZ-RUS, J., ERN, P., ROIG, V. & MARTÍNEZ-BAZÁN, C. 2022 Coalescence of bubbles in a high Reynolds number confined swarm. *J. Fluid Mech.* **944**, A13.
RUTH, D.J., AIYER, A.K., RIVIÈRE, A., PERRARD, S. & DEIKE, L. 2022 Experimental observations and modelling of sub-Hinze bubble production by turbulent bubble break-up. *J. Fluid Mech.* **951**, A32.
SAFFMAN, P.G. 1967 The large-scale structure of homogeneous turbulence. *J. Fluid Mech.* **27** (3), 581–593.
SAFFMAN, P.G.F. & TURNER, J.S. 1956 On the collision of drops in turbulent clouds. *J. Fluid Mech.* **1** (1), 16–30.
SAJJADI, B., RAMAN, A.A.A., SHAH, R.S.S.R.E. & IBRAHIM, S. Review on applicable breakup/coalescence models in turbulent liquid-liquid flows. *Rev. Chem. Engng* **29**, 131–158.
SALIBINDLA, A.K.R., MASUK, A.U.M., TAN, S. & NI, R. 2020 Lift and drag coefficients of deformable bubbles in intense turbulence determined from bubble rise velocity. *J. Fluid Mech.* **894**, A20.
SCARBOLO, L., BIANCO, F. & SOLDATI, A. 2015 Coalescence and breakup of large droplets in turbulent channel flow. *Phys. Fluids* **27**, 073302.
SCIACCHITANO, A. & WIENEKE, B. 2016 PIV uncertainty propagation. *Meas. Sci. Technol.* **27**, 084006.
SEAL, A., DAS, A. & SEN, P. 2015 Watershed: an image segmentation approach. *Intl J. Comput. Sci. Inform. Technol.* **6** (3), 2295–2297.
SERIZAWA, A., KATAOKA, I. & MICHIYOSHI, I. 1975 Turbulence structure of air-water bubbly flow–I. measuring techniques. *Intl J. Multiphase Flow* **2** (3), 221–233.
SHAWKAT, M.E., CHING, C.Y. & SHOUKRI, M. 2008 Bubble and liquid turbulence characteristics of air–water bubbly flow in a large-diameter vertical pipe. *Intl J. Multiphase Flow* **34** (8), 767–785.
SHI, P. 2024 Reversal of the transverse force on a spherical bubble rising close to a vertical wall at moderate-to-high Reynolds numbers. *Phys. Rev. Fluids* **9** (2), 023601.
SHI, P. & MAGNAUDET, J. 2020 Hydrodynamic interaction between a spherical bubble and a wall at finite Reynolds number. *Phys. Fluids* **32** (6), 063304.
SOLIGO, G., ROCCON, A. & SOLDATI, A. 2019 Breakage, coalescence and size distribution of surfactant-laden droplets in turbulent flow. *J. Fluid Mech.* **881**, 244–282.
SREENIVASAN, K.R. 1984 On the scaling of the turbulence energy dissipation rate. *Phys. Fluids* **27** (5), 1048–1051.
TAN, S., ZHONG, S., QI, Y., XU, X. & NI, R. 2025 Dynamics of bubble collision and coalescence in three-dimensional turbulent flows. *J. Fluid Mech.* **1020**, A15.
TAQIEDDIN, A., NAZARI, R., RAJIC, L. & ALSHAWABKEH, A. 2017 Physicochemical hydrodynamics of gas bubbles in two phase electrochemical systems. *J. Electrochem. Soc.* **164** (13), E448.
TAVOULARIS, S. & CORRSIN, S. 1981 Experiments in nearly homogeneous turbulent shear flow with a uniform mean temperature gradient. *J. Fluid Mech.* **104**, 311–347.
TAYLOR, G.I. 1938 The spectrum of turbulence. *Proc. R. Soc. Lond. Series A Math. Phys. Sci.* **164**, 476–490.
TOMIYAMA, A. 1998 Struggle with computational bubble dynamics. *Multiphase Sci. Technol.* **10** (4), 369–405.
TOMIYAMA, A., TAMAI, H., ZUN, I. & HOSOKAWA, S. 2002 Transverse migration of single bubbles in simple shear flows. *Chem. Engng Sci.* **57** (11), 1849–1858.
VALENTE, P.C. & VASSILICOS, J.C. 2012 Universal dissipation scaling for non-equilibrium turbulence. *Phys. Rev. Lett.* **108** (21), 214503.
VAN DEN, B., THOMAS, H., LUTHER, S., LATHROP, D.P. & LOHSE, D. 2006 Bubbly turbulent drag reduction is a boundary layer effect. *J. Turbul.* **7** (14), 1–12.
VAN DEN, B., THOMAS, H., RENSEN, J.M., LUTHER, S. & LOHSE, D. 2020 Bubbles increase turbulent energy dissipation in dilute bubbly flows. *J. Fluid Mech.* **859**, R5.
VELA-MARTÍN, A. & AVILA, M. 2022 Memoryless drop breakup in turbulence. *Sci. Adv.* **8** (50), abp9561.
VERWEY, C. & BIROUK, M. 2022 Dissipation rate estimation in a highly turbulent isotropic flow using 2D-PIV. *Flow Turbul. Combust.* **109**, 647–665.
WANG, H., YANG, W., YAN, X., WANG, L., WANG, Y. & ZHANG, H. 2020 Regulation of bubble size in flotation: a review. *J. Environ. Chem. Engng* **8** (5), 104070.
WESTERWEEL, J. & SCARANO, F. 2005 Universal outlier detection for PIV data. *Exp. Fluids* **39**, 1096–1100.

https://doi.org/10.1017/jfm.2026.11410 Published online by Cambridge University Press

WIENEKE, B. 2015 PIV uncertainty quantification from correlation statistics. *Meas. Sci. Technol.* **26**, 074002.
WILSON, P.L. & SMITH, F.T. 2007 The development of the turbulent flow in a bent pipe. *J. Fluid Mech.* **578**, 467–494.
XU, D. & CHEN, J. 2013 Accurate estimate of turbulent dissipation rate using PIV data. *Exp. Therm. Fluid Sci.* **44**, 662–672.
YANG, C., SUN, Y., YANG, X., XING, Y. & GUI, X. 2025 Analyzing flotation bubble breakup behavior in stirring equipment based on SST k-ω model and VOF model. *Intl J. Coal Prep. Util.* **46**, 1–18.
ZENIT, R. & MAGNAUDET, J. 2008 Path instability of rising spheroidal air bubbles: a shape-controlled process. *Phys. Fluids* **20** (6), 061702.
ZHANG, J., LI, Y., VAFAI, K. & ZHANG, Y. 2018 An investigation of the flow characteristics of multistage multiphase pumps. *Intl J. Numer. Meth. Heat Fluid Flow* **28** (3), 763–784.
ZIKANOV, O., KRASNOV, D., BOECK, T., ZIEGLER, D.P. & THESS, A. 2019 Decay of turbulence in a liquid metal duct flow with transverse magnetic field. *J. Fluid Mech.* **883**, A20.

https://doi.org/10.1017/jfm.2026.11410 Published online by Cambridge University Press